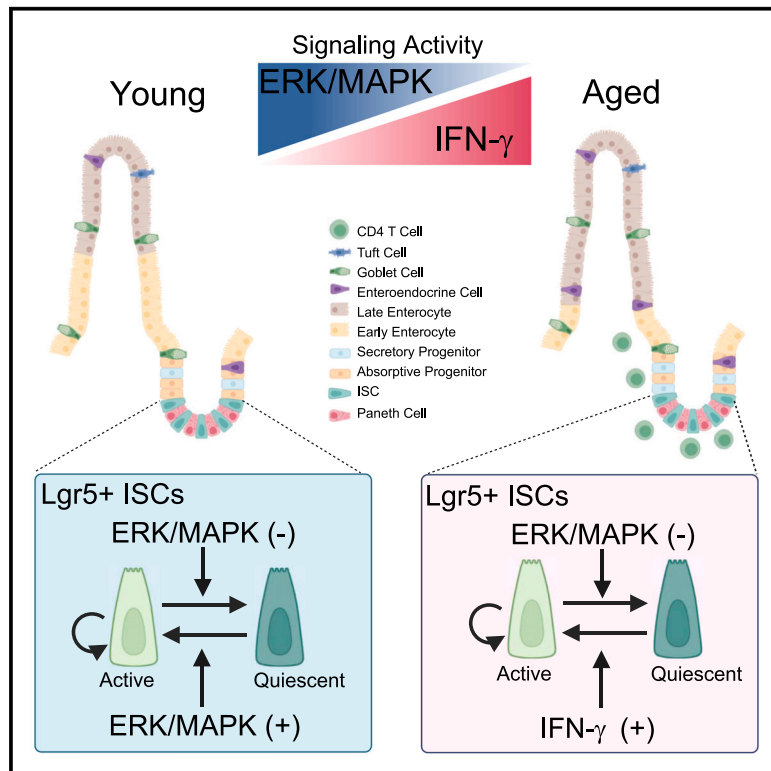


The balance between IFN- γ and ERK/MAPK signaling activities ensures lifelong maintenance of intestinal stem cells

Graphical abstract



Authors

May Nakajima-Koyama, Mio Kabata, Joonseong Lee, ..., Mitinori Saitou, Eisuke Nishida, Takuya Yamamoto

Correspondence

may.koyama@cira.kyoto-u.ac.jp (M.N.-K.), takuya@cira.kyoto-u.ac.jp (T.Y.)

In brief

Nakajima-Koyama et al. report an aging-induced signaling mechanism, which is dependent on the synchronized activation of IFN- γ and inactivation of ERK/MAPK signaling pathways and that functions to maintain an equilibrium between active and quiescent states of Lgr5⁺ intestinal stem cells during aging.

Highlights

- IFN- γ and ERK/MAPK signaling activities alter upon aging in the small intestine
- The balanced activities between IFN- γ and ERK/MAPK signaling maintain the ISC pool
- An equilibrium between the active and the quiescent states exists in the aged ISCs
- Changes in the two signaling pathways affect functions of differentiated cells

Article

The balance between IFN- γ and ERK/MAPK signaling activities ensures lifelong maintenance of intestinal stem cells

May Nakajima-Koyama,^{1,2,*} Mio Kabata,¹ Joonseong Lee,^{1,3} Yuko Sogabe,¹ Satoko Sakurai,¹ Akira Hirota,² Mizuki Kimura,² Tomonori Nakamura,^{3,4,5} Yusuke Imoto,³ Kohei Kometani,¹ Yoko Hamazaki,^{1,6} Yasuaki Hiraoka,³ Mitinori Saitou,^{1,3,4} Eisuke Nishida,^{2,7} and Takuya Yamamoto^{1,3,8,9,*}

¹Center for iPS Cell Research and Application (CiRA), Kyoto University, 53 Kawahara-cho, Shogoin, Sakyo-ku, Kyoto 606-8507, Japan

²Department of Cell and Developmental Biology, Graduate School of Biostudies, Kyoto University, Kitashirakawa-Oiwake-cho, Sakyo-ku, Kyoto 606-8502, Japan

³Institute for the Advanced Study of Human Biology (ASHBi), Kyoto University, Yoshida-Konoe-cho, Sakyo-ku, Kyoto 606-8501, Japan

⁴Department of Anatomy and Cell Biology, Graduate School of Medicine, Kyoto University, Yoshida-Konoe-cho, Sakyo-ku, Kyoto 606-8501, Japan

⁵Hakubi Center for Advanced Research, Kyoto University, Yoshida-Konoe-cho, Sakyo-ku, Kyoto 606-8501, Japan

⁶Laboratory of Immunobiology, Graduate School of Medicine, Kyoto University, 53 Kawahara-cho, Shogoin, Sakyo-ku, Kyoto 606-8507, Japan

⁷RIKEN Center for Biosystems Dynamics Research (BDR), Minatogima-minamimachi, Chuo-ku, Kobe 650-0047, Japan

⁸Medical-Risk Avoidance Based on iPS Cells Team, RIKEN Center for Advanced Intelligence Project (AIP), Kyoto 606-8507, Japan

⁹Lead contact

*Correspondence: may.koyama@cira.kyoto-u.ac.jp (M.N.-K.), takuya@cira.kyoto-u.ac.jp (T.Y.)

<https://doi.org/10.1016/j.celrep.2025.115286>

SUMMARY

While the intestinal epithelium has the highest cellular turnover rates in the mammalian body, it is also considered one of the tissues most resilient to aging-related disorders. Here, we reveal an innate protective mechanism that safeguards intestinal stem cells (ISCs) from environmental conditions in the aged intestine. Using *in vivo* phenotypic analysis, transcriptomics, and *in vitro* intestinal organoid studies, we show that age-dependent activation of interferon- γ (IFN- γ) signaling and inactivation of extracellular signal-regulated kinase/mitogen-activated protein kinase (ERK/MAPK) signaling are responsible for establishing an equilibrium of Lgr5⁺ ISCs—between active and quiescent states—to preserve the ISC pool during aging. Furthermore, we show that differentiated cells have different sensitivities to each of the two signaling pathways, which may induce aging-related, functional, and metabolic changes in the body. Thus, our findings reveal an exquisitely balanced, age-dependent signaling mechanism that preserves stem cells at the expense of differentiated cells.

INTRODUCTION

The mammalian intestinal epithelium has the highest cellular turnover rate in the adult body. This is achieved through the active cycling of intestinal stem cells (ISCs), specifically expressing LGR5, that divide continuously to produce rapidly cycling transit-amplifying (TA) cells, which further differentiate into either absorptive enterocytes or one of four types of secretory cells (Paneth, goblet, tuft, or enteroendocrine cells).^{1,2} The ability of ISCs to self-renew and differentiate and their capacity to regenerate tissues are dependent on multiple signaling pathways.³ These extrinsic signals are released from the stem cell niche, which includes Paneth cells and subepithelial mesenchymal cells, as well as from nearby immune cells.^{4–8} During the lifespan of an organism, the intestinal milieu changes with age, characterized by gut microbiome dysbiosis and immune cell activation, leading to altered intestinal permeability and systemic inflamma-

tion.^{9,10} These aging-related changes in stem cell microenvironments should affect the function of ISCs. Although the regenerative capacity of ISCs is impaired with age,^{11–18} remarkably, they continue to support cell turnover throughout life, suggesting that aging has minimal impact on ISCs in a homeostatic state. This suggests that a protective mechanism may exist that safeguards ISCs from microenvironmental conditions in the aged gut; however, whether such a mechanism actually exists remains unclear.

Here, we describe a mechanism that preserves the ISC population mediated via the synchronized, progressive activation of interferon- γ (IFN- γ) and inactivation of extracellular signal-regulated kinase/mitogen-activated protein kinase (ERK/MAPK) signaling pathways during aging. The previous reports using young mice showed that the activation of the IFN- γ signaling pathway elicits stem cell death,^{18–20} while the inactivation of the ERK/MAPK pathway induces dysregulated cell differentiation.^{21,22} Either of the alterations in the two pathways

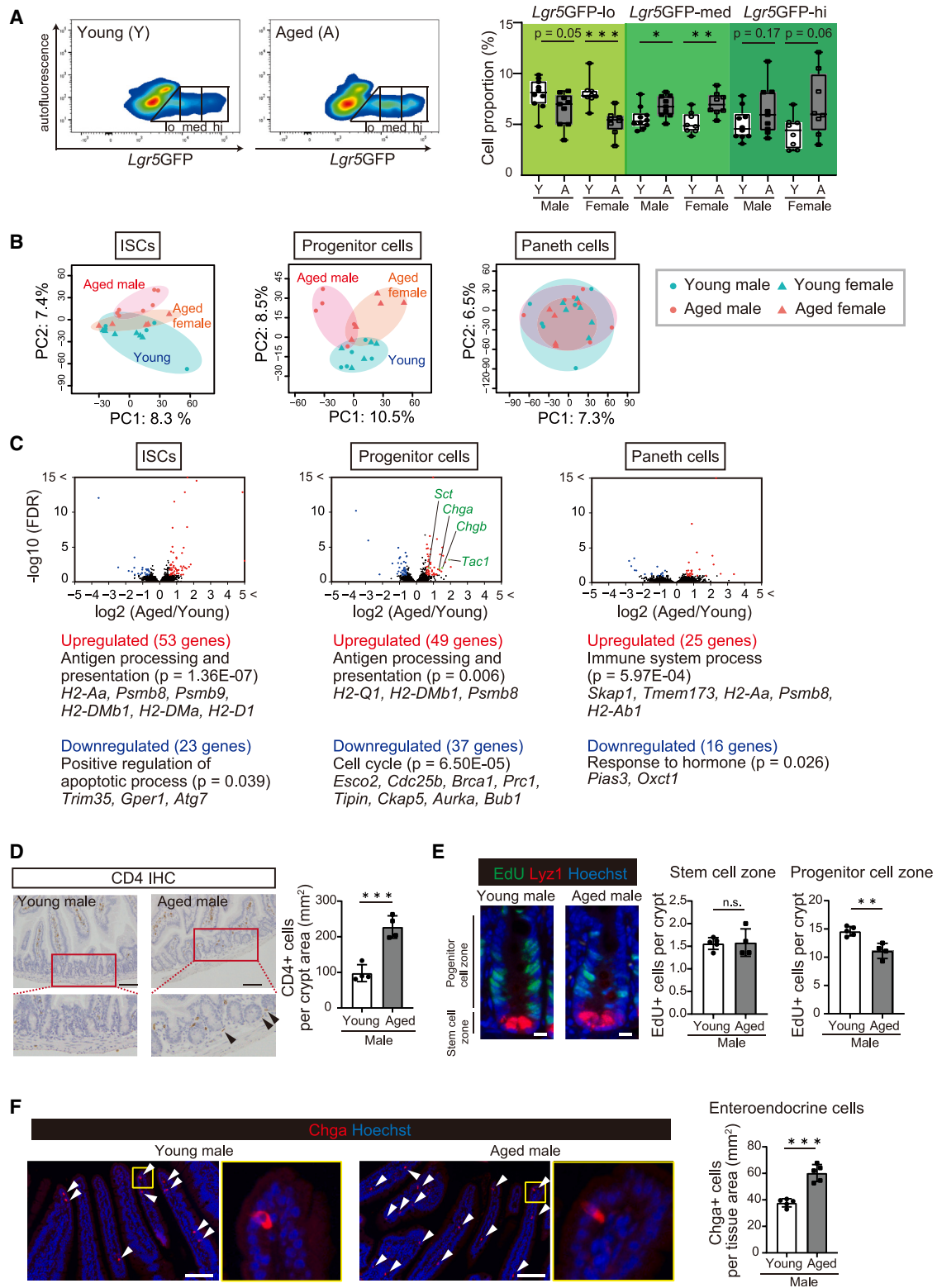


Figure 1. Aging impacts on ISC self-renewal and differentiation

(A) *Lgr5GFP* expression in young and aged intestinal epithelial cells, measured by flow cytometry. Gating was for *Lgr5GFP*^{high} cells (hi), *Lgr5GFP*^{medium} cells (med), and *Lgr5GFP*^{low} (lo) cells. Percentage of *Lgr5GFP*^{low}, *Lgr5GFP*^{medium}, and *Lgr5GFP*^{high} cells in young (Y) mice (male, $n = 10$; female, $n = 8$) and aged

(legend continued on next page)

alone causes severe defects in intestinal homeostasis. Notably, however, when these two conditions are combined, they compensate each other, thereby modulating the balance between active and quiescent states of Lgr5⁺ ISCs to safeguard the ISC pool in aged mice. Conversely, the intestinal organoid model reveals that enteroendocrine cells, enterocytes, and goblet cells have different sensitivities to each signaling pathway; thus, the two age-entrained signaling regulations cannot prevent the age-related alteration in these cell types, which might lead to metabolic changes throughout the body. Our study suggests that the synchronized alterations in the age-related signaling pathways achieve an appropriate balance of ISC regulation, while the alterations induce functional changes in differentiated cells during aging.

RESULTS

Aging affects the ISC differentiation process

We first characterized the intestinal epithelium of young mice (2–4 months of age) and aged mice (22–27 months of age). We observed a slight increase (115%) in crypt height with age under homeostatic conditions (Figure S1A). Consistent with previous studies,^{11,13,15,16,18} we observed impaired tissue regenerative capacity with aging (Figure S1B). Next, by using ethynyl deoxyuridine (EdU) tracing, we observed that intestinal epithelium turnover rate becomes slower with aging (Figure S1C). Furthermore, we observed that the number of ISCs, defined by Olfm4 expression,²³ did not change with aging (Figure S1D). However, the analysis using Lgr5-eGFP-IRES-CreERT2 reporter mice¹ showed that the distributions of Lgr5GFP expression levels change with aging. The proportion of cells with Lgr5GFP^{high} and Lgr5GFP^{medium} tends to increase with age, whereas the proportion of cells with Lgr5GFP^{low} decreases (Figures 1A and S1E).

To explore the molecular basis underlying the effects of aging on ISC self-renewal and differentiation, we performed bulk RNA sequencing (RNA-seq) analysis on isolated Lgr5GFP^{high} (ISCs), Lgr5GFP^{medium/low} (progenitor cells), and Lgr5GFP^{negative}/CD24^{high} niche cells (Paneth cells) from young and aged mice (Figure S1F). Principal-component analysis (PCA) of ISCs and progenitor cells revealed aging-related changes (Figure 1B, PC2 direction), with aged male mice showing a more robust aging signature than aged female mice. Paneth cells did not show any

aging-related changes in the major PC axes. Next, we looked at differentially expressed genes (DEGs) between young and aged mouse-derived cells (Figure 1C; Table S1). Gene Ontology (GO) analysis identified antigen processing and presentation pathway-related genes that were enriched among age-dependent upregulated genes, including major histocompatibility complex (MHC) class II genes such as *H2-Aa*, *H2-DMb1*, *H2-DMA*, and *H2-Ab1* (Figure 1C; Table S1). Interestingly, age-dependent upregulation of MHC class II genes was prominent in male mice (Figure S1G). Furthermore, we also observed increased infiltration of helper T cells into the crypt-surrounding area upon aging (Figure 1D). A recent study has shown that MHC class II expression on ISCs of young mice facilitates antigen presentation to helper T cells, influencing ISC functionality.⁸ Therefore, our results suggest potentially enhanced interactions of crypt epithelial cells, including ISCs and progenitor cells, with helper T cells in the aged intestine. The GO analysis of age-dependent downregulated genes in progenitor cells identified the enrichment of cell-cycle genes (Figure 1C). EdU chase experiments confirmed a reduced number of EdU-positive cells in the aged progenitor cell zone (upper crypt), although not in the stem cell zone (crypt base) (Figure 1E). We also observed several enteroendocrine cell markers (*Tac1*, *Chgb*, *Chga*, and *Sct*) among the age-dependent upregulated genes in progenitor cells (Figure 1C). Indeed, immunohistochemistry for Chga showed a significant increase in enteroendocrine cell number upon aging (Figure 1F). We did not observe any aging-related changes in cell number for other secretory cell types (Figures S1H–S1J). These results indicate that alterations in ISC differentiation processes upon aging lead to shifts in the distribution of Lgr5GFP expression. Moreover, our transcriptome analysis implies that the immune responses within intestinal epithelial cells could be associated with the age-dependent changes in cell proliferation and differentiation.

Aging induces cell-type-specific changes in the intestinal epithelium

Next, we performed single-cell RNA-seq (scRNA-seq) on isolated crypt intestinal epithelial cells. We profiled 10,844 individual cells (5,135 and 5,709 cells from three young mice and three aged mice, respectively). Ten cell types were clustered and annotated by cell-type-specific markers (Figure 2A), which covered most of the cell types in the intestinal epithelium.

(A) mice (male, $n = 9$; female, $n = 8$) is shown. In the boxplots, the line represents the median, the box shows the interquartile range, and the whiskers show the range. *** $p < 0.001$, ** $p < 0.01$, and * $p < 0.05$ by two-tailed Welch's t test.

(B) PCA of bulk-population RNA sequencing of ISCs, progenitor cells, and Paneth cells (young ISCs [male, $n = 5$; female, $n = 6$], aged ISCs [male, $n = 7$; female, $n = 5$], young progenitor cells [male, $n = 5$; female, $n = 5$], aged progenitor cells [male, $n = 5$; female, $n = 5$], young Paneth cells [male, $n = 6$; female, $n = 6$], and aged Paneth cells [male, $n = 7$; female, $n = 5$]).

(C) Volcano plots of differentially expressed genes between young and aged cells (top). GO analysis of age-dependent upregulated/downregulated genes in each cell type (bottom). Age-dependent upregulated enteroendocrine cell markers are shown in green.

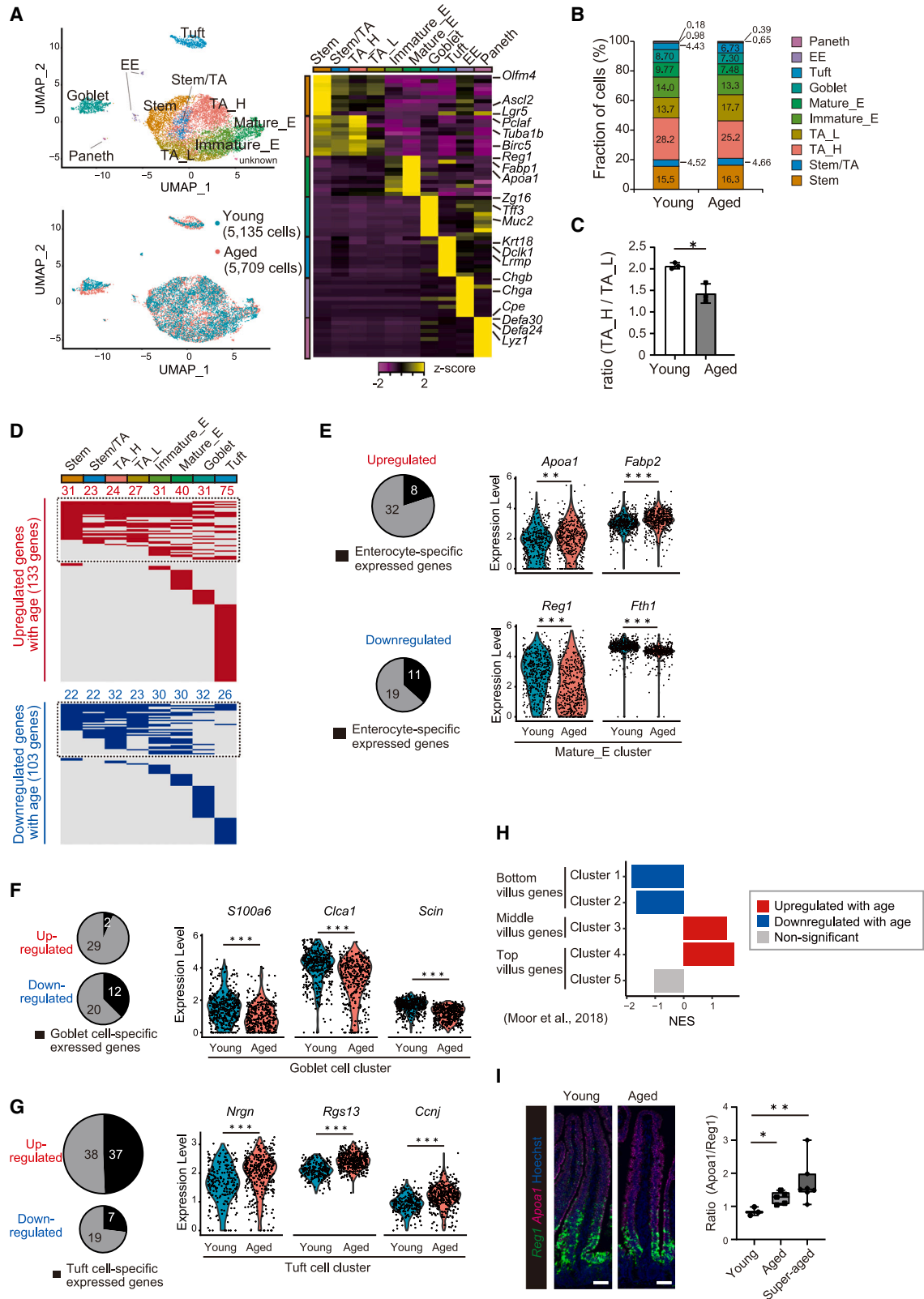
(D) Representative images of anti-CD4 antibody staining (left). Scale bars, 100 μm . Magnified areas (red box) are shown below. CD4-positive cells located near the crypt base are indicated by black arrowheads. Quantification of CD4-positive helper T cells per crypt area (young male, $n = 4$; aged male, $n = 4$) (right).

(E) Representative images of EdU and anti-Lyz1 (Paneth cell marker) antibody staining at 4 h post-EdU treatment. The stem cell zone is defined as a crypt base adjacent to Lyz1-positive Paneth cells, and the progenitor cell zone is defined as an upper crypt area. Scale bars, 10 μm . Quantification of EdU-positive cells in the stem cell zone or the progenitor cell zone (young male, $n = 5$; aged male, $n = 4$).

(F) Representative images of anti-Chga antibody staining. Chga-positive cells are indicated by arrowheads. Magnified images of the indicated areas (yellow) are shown on the right. Scale bars, 100 μm . Quantification of Chga-positive cells per tissue area (young male, $n = 5$; aged male, $n = 5$).

(D–F) *** $p < 0.001$, ** $p < 0.01$, and n.s., not significant by two-tailed Welch's t test. Data are presented as the mean \pm SD.

See also Figure S1 and Table S1.



(legend on next page)

However, the observed proportions of Paneth cells (0.18% for young mice and 0.39% for aged mice) and enteroendocrine cells (0.98% for young mice and 0.65% for aged mice) were lower than expected, based on a previous study²⁴ (3.6% for Paneth cells and 4.3% for enteroendocrine cells in young mice) (Figure 2B). This discrepancy may be due to their susceptibility to the stress induced during single-cell dissociation, which could impact our measurement accuracy of age-related changes in the Paneth and enteroendocrine cell population. For other cell types, we noticed that cell identities were overall largely maintained with aging (Figure 2B). However, the ratio of the high-proliferative TA cells to low-proliferative TA cells was decreased after aging (Figure 2C), consistent with our phenotypic analysis (Figure 1E). Next, we characterized aging-related features based on DEGs in each cell type (Figure 2D; Tables S2 and S3). Many age-dependent DEGs in stem cells were shared with those in TA cells (Figure 2D). In contrast, terminally differentiated cells, such as mature enterocytes, goblet cells, and tuft cells, exhibited cell-type-specific transcriptional changes associated with aging (Figure 2D), suggesting that aging might affect the maturation and functionality of these cells (Figures 2E–2G; Table S3). Previous studies have shown that enterocytes undergo maturation as they transition from the crypt to the top of the villus.²⁵ Interestingly, gene set enrichment analysis (GSEA) identified a shift in gene expression profiles from the bottom villus profiles in young intestinal epithelia to the middle-to-top villus profiles in aged intestinal epithelia (Figure 2H). These results were further confirmed by RNA *in situ* hybridization for *Reg1* (a bottom villus gene) and *Apoa1* (a top villus gene) (Figure 2I). Our findings indicate that enterocyte maturation becomes enhanced with aging. Moreover, we also observed an age-dependent upregulation in metabolically related genes in enterocytes, such as the lipid transporter gene *Fabp2* and apolipoprotein genes (*Apoa1*, *Apoc3*, *Apob*, and *Apoa4*) (Figure 2E; Table S3). This suggests that aging may result in a metabolic shift of enterocytes.

Collectively, our transcriptome analyses revealed that aging-related changes occur in a cell-type-specific manner, even though the overall intestinal epithelial cell identity is maintained.

Identification of aging markers for the intestinal epithelium

The GO analysis with our scRNA-seq data revealed that genes related to antigen processing and presentation were upregulated upon aging in intestinal epithelial cells (Figure 3A), consistent with the bulk RNA-seq data (Figure 1C). In particular, four MHC class II genes (*H2-Aa*, *H2-Eb1*, *H2-Ab1*, and *Cd74*) are included among the top 10 age-dependent upregulated genes in ISCs (Figure 3B; Table S3). Next, we integrated our scRNA-seq dataset with that of previous studies^{18,26} (Figures S2A–S2D) to identify genes commonly up-/downregulated with age in the ISC populations (Figures S2E and S2F). Consistent with previous studies,^{18,26} genes related to antigen processing and presentation were commonly upregulated with age (Figure S2E). Moreover, we found that two genes, *Ceacam10* and *Ly6e*, exhibit prominent age-dependent upregulation, comparable to the extent observed in MHC class II genes in ISCs (Figures 3B and S2E), which was also confirmed by our bulk RNA-seq analysis (Figure 3C). Aging-related upregulation of MHC class II genes, *Ceacam10*, and *Ly6e* in intestinal epithelial cells was also previously observed in transcriptome/proteome data.^{11,17,27} Therefore, these genes could be reliable aging markers of the intestinal epithelium.

RNA *in situ* hybridization analysis validated the upregulation of these aging markers in aged mouse intestinal epithelium (Figure 3D). We found distinct expression patterns among these aging markers in the tissue; *H2-Aa* expression was much higher in the villi than in the crypts, whereas *Ceacam10* and *Ly6e* expression was limited in crypts in aged mice (Figure 3D). Interestingly, our RNA *in situ* hybridization indicated that a subset of

Figure 2. scRNA-seq reveals the cell-type-specific changes upon aging

- (A) Uniform manifold approximation and projection (UMAP) plots for intestinal epithelial cells (young, $n = 5,135$ from 3 male mice; aged, $n = 5,709$ from 3 male mice) (left). Cell-type clusters (upper left). Stem/TA, intermediates between stem cells and transit-amplifying (TA) cells; TA_H, high-proliferative TA cells; TA_L, low-proliferative TA cells; Immature_E, immature enterocytes; Mature_E, mature enterocytes; EE, enteroendocrine cells. The distribution of young and aged cells (lower left). Heatmap of cell-type markers (right). The relative expression levels (Z score) of cell-type markers (rows) across the cell clusters (columns) are shown.
- (B) The proportion of each cell type.
- (C) The ratio of TA_H cells to TA_L cells (young male, $n = 3$; aged male, $n = 3$). * $p < 0.05$ by two-tailed Welch's t test. Data are presented as the mean \pm SD.
- (D) Heatmaps for the distribution of age-dependent upregulated (top, red) and downregulated (bottom, blue) genes in each intestinal epithelial cell type. Genes not differentially expressed with age are shown in gray. Dotted lines indicate the age-dependent DEGs shared by at least two cell types. The lower part represents the unique DEGs in each cell type. The numbers of age-dependent up-/downregulated genes in each cell type are shown at the top of each column.
- (E) The numbers of age-dependent up-/downregulated genes in mature enterocytes (left). Enterocyte-specific expressed genes are shown in black. Violin plots of *Apoa1* and *Fabp2* as age-dependent upregulated enterocyte-specific expressed genes and *Reg1* and *Fth1* as age-dependent downregulated enterocyte-specific expressed genes in the mature enterocyte population (right). **adjusted $p < 0.01$, ***adjusted $p < 0.001$.
- (F) The numbers of age-dependent up-/downregulated genes in goblet cells (left). Goblet cell-specific expressed genes are shown in black. Violin plots of age-dependent downregulated goblet cell-specific expressed genes (*S100a6*, *C1ca1*, and *Scin*) (right). ***adjusted $p < 0.001$.
- (G) The numbers of age-dependent up-/downregulated genes in tuft cells (left). Tuft cell-specific expressed genes are shown in black. Violin plots of age-dependent upregulated tuft cell-specific expressed genes (*Nrgn*, *Rgs13*, and *Ccnj*) (right). ***adjusted $p < 0.001$.
- (H) Gene set enrichment analysis on young and aged mature enterocytes. Genes were compared against the zonation-dependent gene sets reported in the previous study.²⁵ Cluster 1 represents the bottom villus-enriched genes and cluster 5 represents the top villus-enriched genes. Normalized enrichment score (NES) is shown. Bars in red indicate significant enrichment of age-dependent upregulated genes at false discovery rate (FDR) < 0.05 , bars in blue indicate significant enrichment of age-dependent downregulated genes at FDR < 0.05 , and bars in gray represent gene sets with no significance (FDR > 0.05).
- (I) Representative images of *Reg1* (green) and *Apoa1* (magenta) RNA *in situ* hybridization (left). Scale bars, 50 μm . The ratio between *Reg1* and *Apoa1* signal intensities in villi (right). Young male, $n = 3$; aged male, $n = 5$; super-aged male, $n = 6$. * $p < 0.05$ and ** $p < 0.01$ by two-tailed Welch's t test. In the boxplots, the line represents the median, the box shows the interquartile range, and the whiskers show the range.
- See also Table S2 and Table S3.

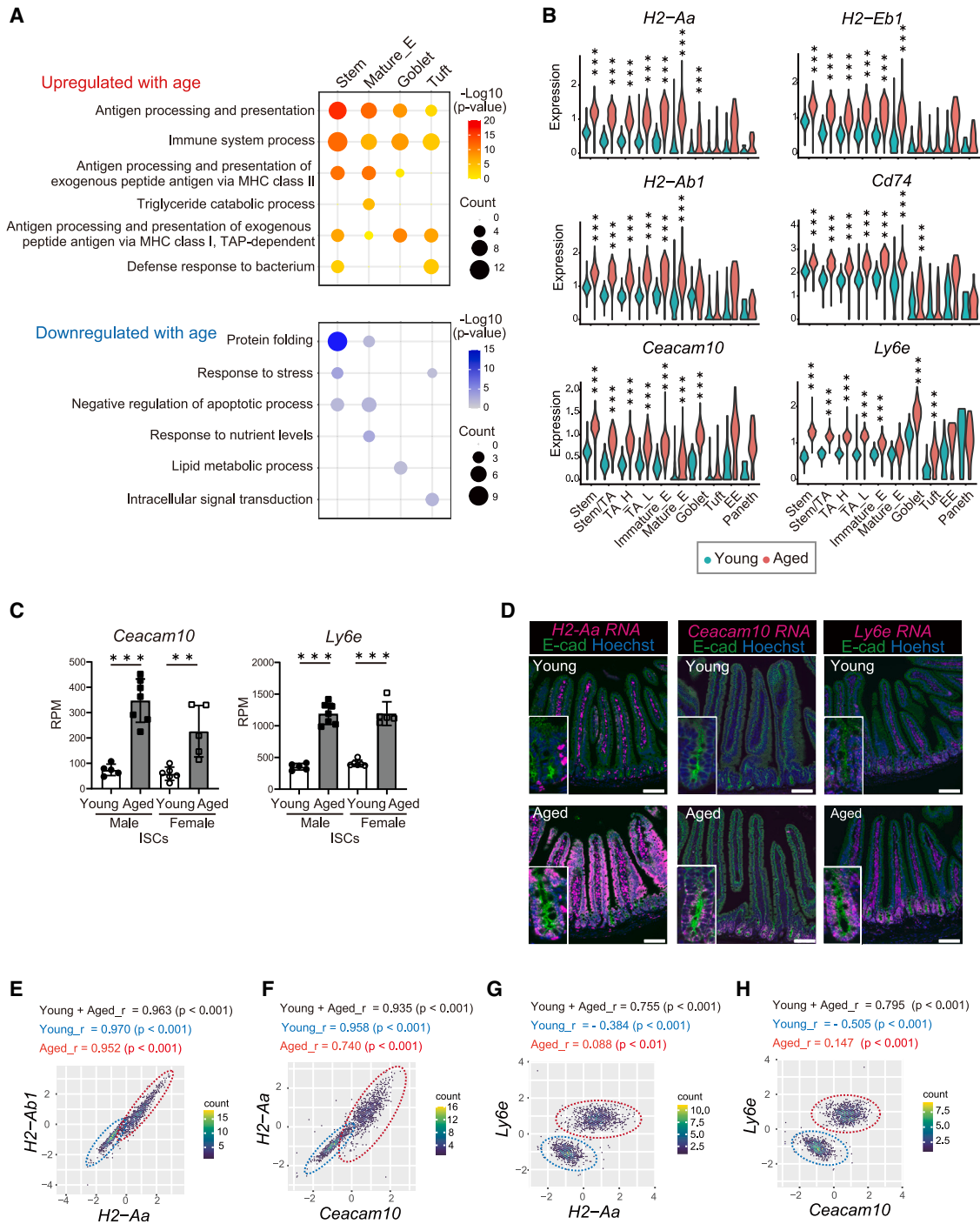


Figure 3. Identification of aging markers of intestinal epithelium

(A) Dot plots for enriched GO terms of age-dependent DEGs in each cell type. The p values are shown in the color range. Counts, indicating gene number, are shown in the dot size.

(B) Violin plots of intestinal aging markers, MHC class II genes (*H2-Aa*, *H2-Eb1*, *H2-Ab1*, and *Cd74*), *Ceacam10*, and *Ly6e*, in each cell type. ***adjusted $p < 0.001$.

(C) Expression levels of the aging markers (*Ceacam10* and *Ly6e*) in ISCs (young [male, $n = 5$; female, $n = 6$] and aged [male, $n = 7$; female, $n = 5$]). RPM (reads per million mapped reads) from bulk population RNA-seq is shown. **FDR < 0.01 and ***FDR < 0.001 . Data are presented as the mean \pm SD.

(D) Representative images of *H2-Aa*, *Ceacam10*, and *Ly6e* (magenta) RNA *in situ* hybridization and anti-E-cadherin antibody staining (green). Magnified images of crypts are shown in the insets. Scale bars, 100 μm . *H2-Aa* and *Ly6e* are also expressed in immune cells of the lamina propria.

(legend continued on next page)

enteroendocrine progenitor cells highly express *Ceacam10* (Figure S3). Our findings suggest that, while all the aging markers are significantly upregulated in the ISCs with age, their expression characteristics vary among the different cell types.

We then looked at the relationship between the aging markers at the single-cell level in the ISC population (Figures 3E–3H). The expression of two MHC class II genes, *H2-Aa* and *H2-Ab1*, showed a strong correlation in both young and aged ISCs, suggesting that common factors might regulate these genes (Figure 3E). Although *H2-Aa* and *Ceacam10* expression showed a strong correlation ($r = 0.958$) in young ISCs, notably, their correlation became weaker ($r = 0.740$) with aging (Figure 3F). The expression of *Ly6e* showed a weak correlation with *H2-Aa* or *Ceacam10* expression in both young and aged ISCs (Figures 3G and 3H). These results likely indicate that *H2-Aa*, *Ceacam10*, and *Ly6e* are regulated by different transcriptional mechanisms.

Collectively, our transcriptome analysis identified the aging markers for the intestinal epithelium; however, MHC class II genes, *Ceacam10*, and *Ly6e* may be regulated by different mechanisms, suggesting that multiple upstream regulators govern the intestinal epithelium aging.

Alterations in IFN- γ and ERK/MAPK signaling activities upon aging

By using Ingenuity Pathway Analysis (IPA, Qiagen), we identified several candidate upstream signaling pathways that were activated and inactivated in aged mice (Figure 4A; Table S4). Since interleukin and chemokine receptors were expressed at low levels in ISCs (Figures 4B, S4A, and S4B), we excluded these pathways from further validation experiments. Based on previous studies,^{13–16} we also screened the mTOR and fatty acid oxidation (FAO) signaling pathways. To test whether the predicted pathways could induce aging-marker expression and aging-related cellular changes, cytokines or chemical compounds mimicking upstream regulatory components were added to the intestinal organoid culture medium (Figure 4C).

Our organoid screen demonstrated that type II IFN, IFN- γ , markedly induced *H2-Aa* expression beyond *in vivo* physiological levels (Figure 4D). Our time-course analysis revealed that *H2-Aa* upregulation occurred as early as 4 h after IFN- γ treatment, and its upregulation was prevented by the JAK1/2 inhibitor ruxolitinib (Figures 4E and S4C). Previous studies have shown that during acute inflammation in young mice, IFN- γ signaling increases the expression of MHC class II genes in intestinal epithelial cells.^{28,29} More recently, studies have also reported that MHC class II genes are directly regulated by the STAT1 transcription factor downstream of the IFN- γ signaling pathway in the aging intestine.^{18,26} In line with these findings, our RT-qPCR analysis confirmed an aging-related increase in *Irfng* mRNA expression at the whole-tissue level (Figure 4F), indicating that activation of IFN- γ signaling during aging upregulates MHC class II gene expression.

Interestingly, previous reports have identified *Ly6e* as an IFN-inducible gene.^{30,31} We found that IFN- γ , type I IFN (IFN- α), or the TLR3 ligand (poly(I:C)) increased *Ly6e* expression in intestinal organoids (Figure 4D). Our time-course analysis revealed that *Ly6e* was upregulated as early as 4 h after IFN- α treatment, whereas IFN- γ and poly(I:C) induced *Ly6e* expression at later time points (Figure 4E). Poly(I:C) treatment also induced type III IFNs, *Irfn2* and *Irfn3*, before *Ly6e* upregulation (Figure S4D). This upregulation of *Ly6e* induced by IFN- α or IFN- λ at 4 h could be suppressed by adding a JAK1/2 inhibitor (Figure S4E). Our results revealed that *H2-Aa* and *Ly6e* exhibit different sensitivities to IFN- γ and IFN- α/λ treatment (Figures 4E, S4C, and S4E). It is known that IFN- γ activates the STAT1 homodimer, whereas IFN- α/λ also activates the STAT1/STAT2 heterodimer to regulate different gene sets.^{32,33} Therefore, *H2-Aa* and *Ly6e* may be induced by distinct types of IFN in the aging intestine. Although RT-qPCR analysis did not detect type I and type III IFN mRNA expression at the whole-tissue level *in vivo*, this is likely due to their low expression levels.

We also observed that IFN- γ decreased *Ceacam10* expression, whereas the MEK/ERK MAPK pathway inhibitor (iMEK) increased *Ceacam10* expression in a dose-dependent manner (Figure 4D). Moreover, only iMEK treatment increased the enteroendocrine cell marker while decreasing the proliferative marker *Ki67* (Figure 4D), reflecting aging-related changes. These findings are consistent with a previous study showing that iMEK increases quiescent Lgr5⁺ ISCs and enhances enteroendocrine cell differentiation in intestinal organoids.²¹

Immunostaining of young intestinal epithelia for phospho-ERK1/2, the active form of ERK/MAPK, represented a mosaic distribution pattern within the intestinal crypts (Figures 4G and S4F), likely due to the oscillatory nature and active propagation of ERK/MAPK signaling in the intestine.³⁴ We found a progressive decrease in phospho-ERK1/2 levels in the crypts with aging (Figures 4G and S4F). These results indicate that aging results in ERK/MAPK signaling inactivation, affecting *Ceacam10* expression as well as cell proliferation and differentiation within the aged intestine. However, the induction of *Ceacam10* expression required a relatively long time (24 and 48 h) after iMEK treatment (Figure 4E), indicating that *Ceacam10* may not be a direct downstream target of ERK/MAPK signaling.

Since the TLR1 ligand Pam3CSK4 also induced *Ceacam10* expression (Figure 4D), we examined whether downstream regulators of TLR signaling, such as p38/MAPK, JNK/MAPK, and NF- κ B, are involved in iMEK-induced *Ceacam10* expression. We found that a p38/MAPK signaling inhibitor suppressed both iMEK- and Pam3CSK4-induced *Ceacam10* expression (Figure S4G). As a previous study demonstrated p38/MAPK signaling activation in the aged intestinal epithelium,¹⁵ our findings suggest that age-dependent ERK/MAPK signaling inactivation may lead to p38/MAPK signaling activation, thereby inducing *Ceacam10* expression.

(E–H) Density scatterplots of intestinal aging marker expression in young and aged mouse-derived ISCs. Expression levels are shown as Z scores using ISCs derived from young mice and aged mice. Plots of young mouse-derived cells are circled by blue dotted lines, and plots of aged mouse-derived cells are circled by red dotted lines. Pearson correlation coefficients and *p* values are shown for ISCs derived from young and aged mice (Young + Aged), young mice only (Young), and aged mice only (Aged).

See also Figure S2 and Figure S3.

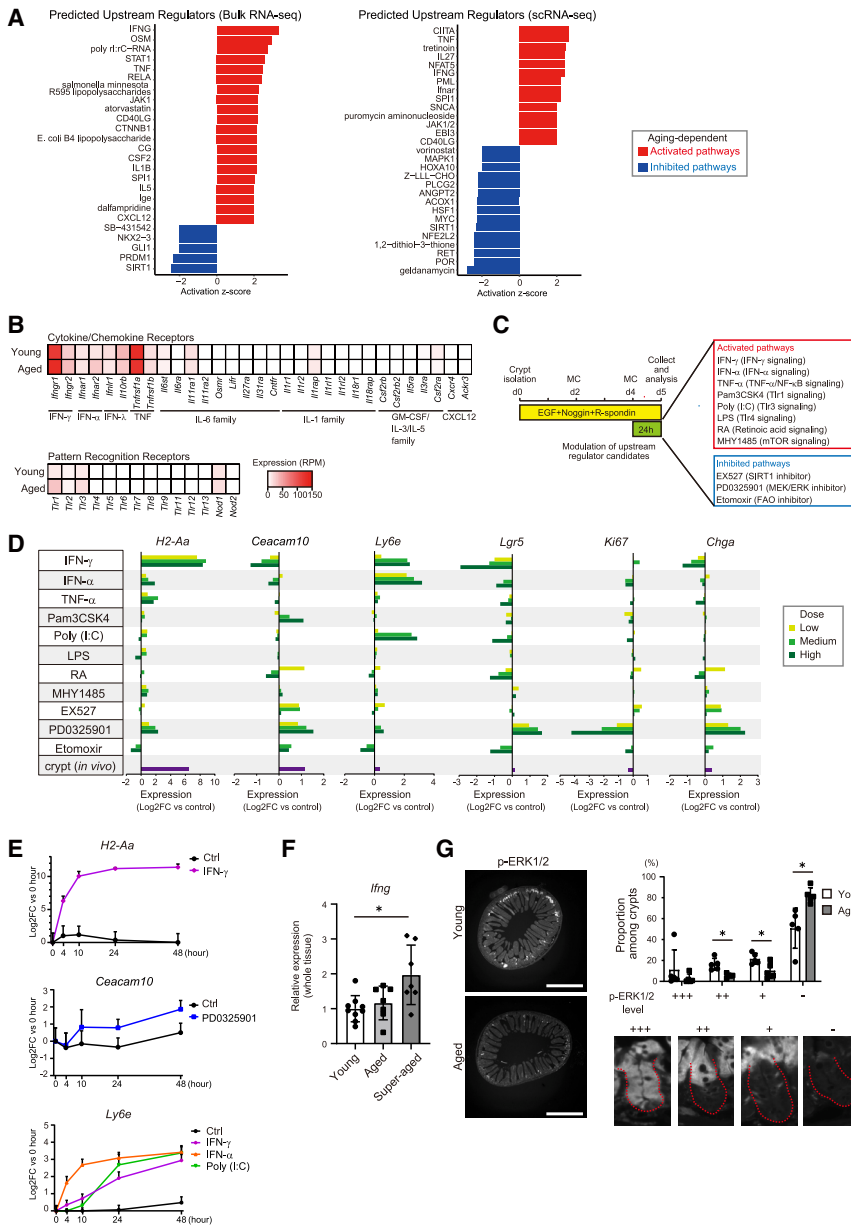


Figure 4. Identification of signaling pathways that induce the aging characteristics in intestinal epithelium

(A) Bar plots for Ingenuity Pathway Analysis (IPA, Qiagen) on ISC bulk population RNA-seq data (left) and stem cell population scRNA-seq data (right). Activation Z scores are shown. Bars in red indicate the predicted aging-dependent activated pathways, and bars in blue indicate the predicted aging-dependent inhibited pathways.

(B) Heatmaps for average expression levels of cytokine/chemokine receptors (top) and pattern recognition receptors (bottom) in *Lgr5*GFP^{high} ISCs (young male, *n* = 5; aged male, *n* = 7). RPM from bulk population RNA-seq is shown in the color range.

(C) Scheme for the screening assay for upstream regulators using intestinal organoids. MC, medium change.

(D) RT-qPCR analysis of *H2-Aa*, *Ceacam10* and *Ly6e* (aging markers), *Lgr5* (ISC marker), *Ki67* (cell proliferative marker), and *Chga* (enteroendocrine cell marker) expression. Cytokines or chemical compounds were added at several doses (see STAR Methods). Expression levels in freshly isolated crypts are also shown (purple). The log fold changes in gene expression relative to the expression in control samples are shown.

(E) RT-qPCR analysis of *H2-Aa*, *Ceacam10*, and *Ly6e*. IFN- γ (0.5 ng/mL), PD0325901 (3 μ M), IFN- α (1 ng/mL), or poly(I:C) (10 μ g/mL) was added for 4, 10, 24, and 48 h (*n* = 4). The log fold changes in gene expression relative to the expression in the 0 h samples are shown. The data are presented as the mean + SD.

(F) RT-qPCR analysis of *Ifng* expression in young, aged, and super-aged mouse small intestines (young male, *n* = 9; aged male, *n* = 7; super-aged male, *n* = 7).

(G) Representative images of anti-phospho-ERK1/2 (p-ERK1/2) antibody staining in transverse sections of the small intestine (left). Scale bars, 1 mm. (Right) p-ERK1/2 levels are divided into four levels (+++, positive in the whole crypt; ++, positive in the upper half of the crypt; +, positive in the peripheral region of the

crypt and villus; -, negative). Crypts are shown as red dotted lines (bottom right). Quantification of p-ERK1/2 levels in the crypts is shown (young male, *n* = 5; aged male, *n* = 5). (F and G) **p* < 0.05 by two-tailed Welch's *t* test. Data are presented as the mean \pm SD. See also Figure S4 and Table S4.

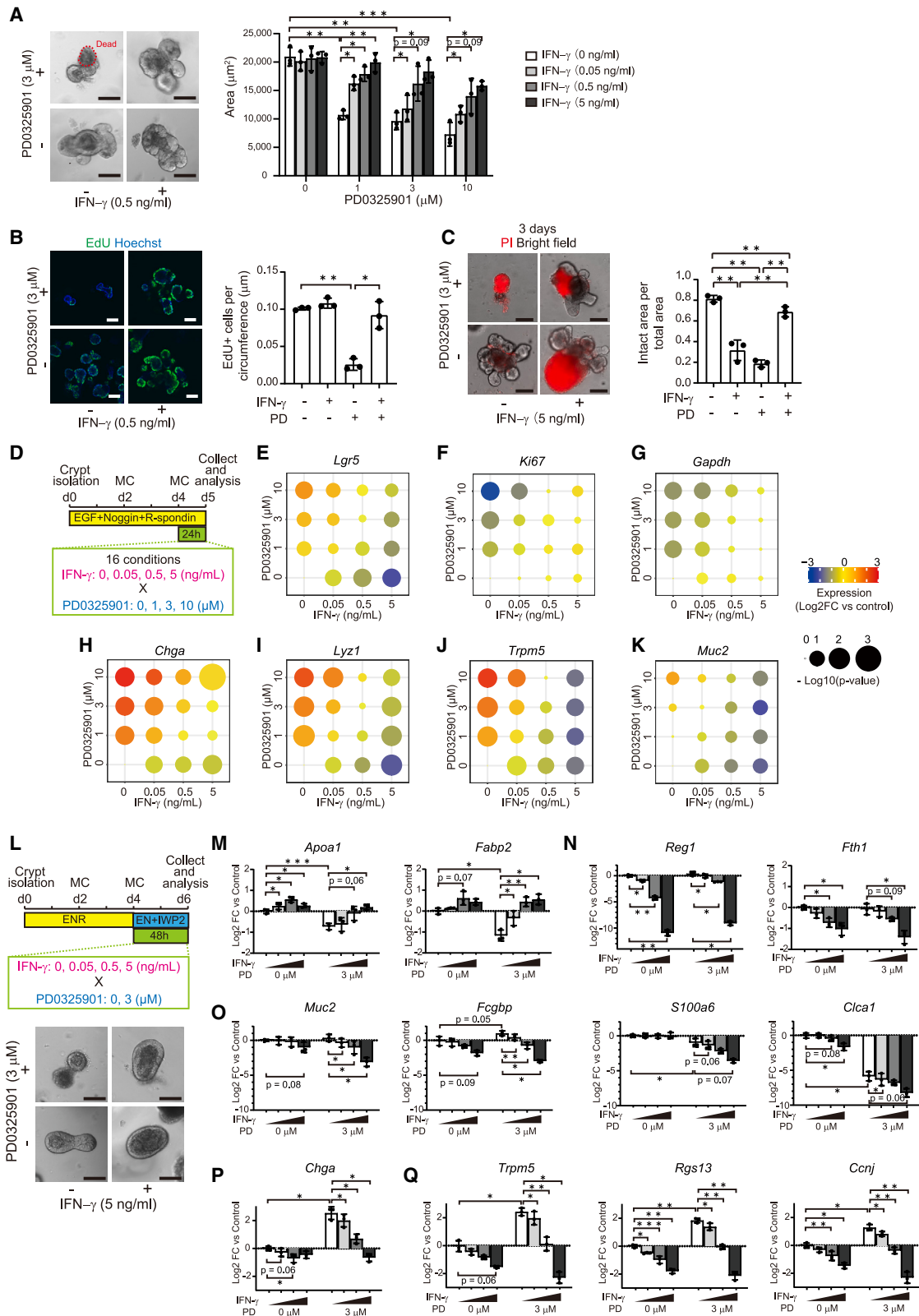
Together, our findings suggest that the activation of IFN- γ signaling and inactivation of ERK/MAPK signaling occur simultaneously in the intestinal epithelium during aging, inducing transcriptional and cellular changes.

The activation of IFN- γ signaling and inactivation of ERK/MAPK signaling act in a compensatory manner to maintain the ISC pool

Previous studies using young mice have shown that T cell-derived IFN- γ is associated with cell death of active ISCs and severe inflammation.^{19,20} Inactivation of the ERK/MAPK pathway

induces ISC quiescence and enteroendocrine cell differentiation while inhibiting differentiation to enterocytes, leading to malnutrition.^{21,22} Hence, the changes in these signaling pathways have negative impacts on intestinal epithelial homeostasis in young mice. However, the combined effects of these signaling activities on intestinal homeostasis are yet to be elucidated.

Therefore, we examined the combined effects of IFN- γ and iMEK treatment on ISCs using intestinal organoids from young mice (Figure 5A). Organoid size did not change with IFN- γ treatment alone. iMEK alone caused a smaller organoid size. Importantly, the addition of IFN- γ rescued the reduced organoid size



(legend on next page)

phenotype resulting from iMEK treatment in a dose-dependent manner. A short pulse of EdU in organoids clearly showed that iMEK induced a quiescent state, but IFN- γ released these cells from this state (Figure 5B). Previous studies have shown that prolonged treatment of high-dose IFN- γ causes organoid death.^{19,20} Notably, our data showed that combining iMEK and high-dose IFN- γ (5 ng/mL) mitigates the organoid damage induced by either single treatment (Figure 5C). The efficiencies of intestinal organoid formation between young and aged mice were similar (Figure S5A), and we also found that the combined effects of IFN- γ and iMEK treatment on organoids derived from aged mice were comparable to those from young mice (Figures S5B–S5D). Collectively, our organoid data suggest that the IFN- γ signaling and ERK/MAPK signaling pathways act in a compensatory manner to maintain the ISC pool in both young and aged mice.

The balance of IFN- γ and ERK/MAPK signaling activities influences intestinal homeostasis

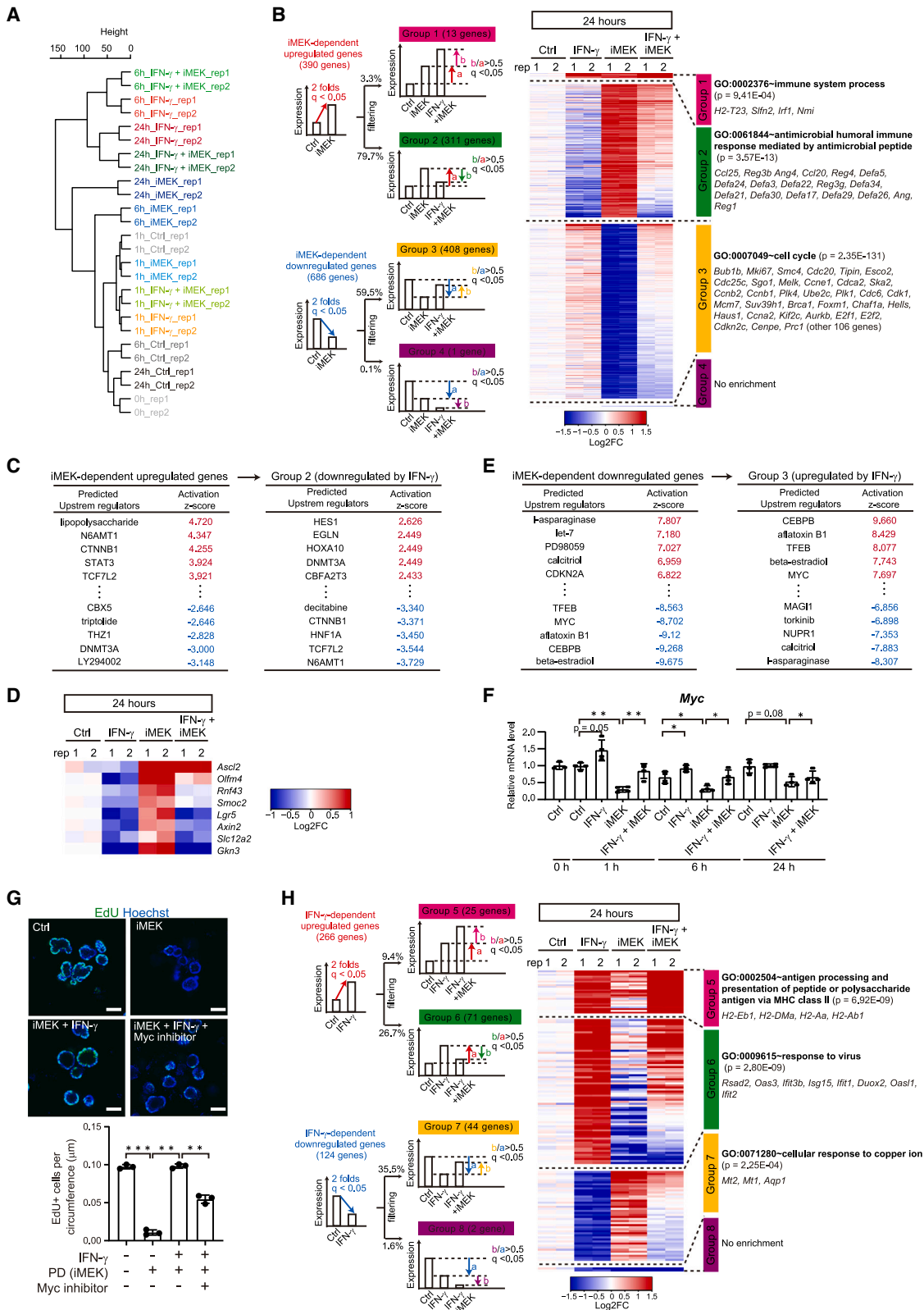
By modulating the balance between the IFN- γ and the ERK/MAPK signaling pathways in our intestinal organoid system, we also observed that some characteristic features are associated with aging in the intestinal epithelium (Figures 5D–5K and S5E–S5K). *Lgr5* was upregulated by iMEK and downregulated by IFN- γ in a dose-dependent manner, and both iMEK and IFN- γ primarily offset these opposing effects (Figures 5E and S5E). At the same time, *Ki67* expression was downregulated by iMEK and rescued by IFN- γ in a dose-dependent manner (Figures 5F and S5F). Moreover, *Gapdh*, a glycolytic enzyme highly expressed in absorptive (enterocyte) lineage, is downregulated by iMEK and rescued by IFN- γ (Figures 5G and S5G). These findings suggest that the optimal balance of iMEK and IFN- γ is critical for maintaining ISCs and their proliferative capacity and enterocyte-lineage commitment at a level similar to that observed under control culture conditions. We also

observed that the marker genes of secretory cell types, including enteroendocrine, Paneth, tuft, and goblet cells, were upregulated by iMEK treatment and downregulated by IFN- γ treatment (Figures 5H–5K and S5H–S5K). Importantly, the sensitivity to iMEK or IFN- γ treatment differed among cell types; *Chga*, an enteroendocrine cell marker, showed higher sensitivity to iMEK and lower sensitivity to IFN- γ than other secretory cell-type markers (Figures 5H–5K and S5H–S5K). These differences in sensitivity to the two signaling pathways in secretory cell differentiation clarify why only enteroendocrine cell numbers were significantly increased in the aged intestine *in vivo* (Figure 1F).

Next, we further investigated the effects of iMEK and IFN- γ treatment on the cell maturation process (Figure 5L). Our results showed that iMEK treatment tended to suppress the expression of *Apoa1* and *Fabp2*, which are genes characteristic of aged enterocytes, and that this suppression was rescued upon IFN- γ addition under the cell differentiation condition (Figures 5M and S5L). On the other hand, the expression of *Reg1* and *Fth1*, which are genes characteristic of young enterocytes, was reduced by IFN- γ treatment (Figures 5N and S5M). These results suggest that IFN- γ predominantly enhances enterocyte maturation toward a more aged phenotype, consistent with the high expression levels of IFN- γ receptors (*Ifngr1* and *Ifngr2*) in mature enterocytes (Figure S4A). In goblet cells, age-dependent downregulated genes, such as *S100a6* and *Ctca1* (Figure 2F), tend to be synergistically suppressed by the combined treatment of iMEK and IFN- γ (Figure 5O). In contrast, pan-goblet marker genes, such as *Muc2* and *Fcgbp*, were exclusively downregulated by IFN- γ treatment (Figure 5O). This result suggests that synchronized alteration in these two signaling activities affects goblet cell functions without changing the number of cells. Consistent with Figure 5H, *Chga*, an enteroendocrine cell marker, showed higher sensitivity to iMEK and lower sensitivity to IFN- γ under the differentiation condition (Figure 5P). We found that both the pan-Tuft cell marker *Trpm5* and age-dependent

Figure 5. The effects of IFN- γ and ERK/MAPK signaling modulation on intestinal organoids derived from young mice

(A) The MEK/ERK MAPK inhibitor PD0325901 (1, 3, or 10 μ M) and/or IFN- γ (0.05, 0.5, or 5 ng/mL) was added to the organoid culture medium for 24 h. Representative images of intestinal organoids (left). Scale bars, 100 μ m. The size of organoids per condition from three independent experiments (right).
(B) PD0325901 (3 μ M) and/or IFN- γ (0.5 ng/mL) was added to the organoid culture medium for 24 h. For the last 2 h, EdU (final 10 μ M) was added to the culture medium. Representative images of EdU-stained intestinal organoids (left). Scale bars, 100 μ m. The number of EdU-positive cells per circumference (μ m) of organoids from three independent experiments (right).
(C) PD0325901 (3 μ M) and/or IFN- γ (5 ng/mL) was added to the organoid culture medium for 3 days. Representative images of propidium iodide (PI) staining in intestinal organoids (left). Scale bars, 100 μ m. The proportion of intact area (PI negative) relative to the total area (PI positive and negative) from three independent experiments (right).
(D) Experimental scheme for (E)–(K). IFN- γ (0.05, 0.5, or 5 ng/mL) and/or PD0325901 (1, 3, or 10 μ M) was added to the culture medium for 24 h.
(E–K) RT-qPCR analysis of *Lgr5* (ISC marker), *Ki67* (cell proliferative marker), *Gapdh* (enterocyte lineage marker), *Chga* (enteroendocrine cell marker), *Lyz1* (Paneth cell marker), *Trpm5* (tuft cell marker), and *Muc2* (goblet cell marker) from three independent experiments. The log fold changes of gene expression relative to the expression in control samples are shown in the color range. The *p* values calculated by paired two-tailed *t* test compared with the control sample are shown in the dot size.
(L) Cell differentiation was induced by removing R-spondin1 and adding IWP2 (EN + IWP2) for 48 h. IFN- γ (0.05, 0.5, or 5 ng/mL) and/or PD0325901 (3 μ M) was added to the culture medium for 48 h. The results are shown in (M)–(Q). Representative images of intestinal organoids (bottom). Scale bars, 100 μ m.
(M) RT-qPCR analysis of age-enriched enterocyte markers (*Apoa1* and *Fabp2*) from three independent experiments. The log fold changes in gene expression relative to the expression in control samples are shown.
(N) RT-qPCR analysis of young-enriched enterocyte markers (*Reg1* and *Fth1*) from three independent experiments. The log fold changes in gene expression relative to the expression in control samples are shown.
(O–Q) RT-qPCR analysis of goblet cell-specific genes (O), enteroendocrine marker (P), and tuft cell-specific genes (Q) from three independent experiments. The log fold changes in gene expression relative to the expression in control samples are shown.
(A–C and M–Q) **p* < 0.05, ***p* < 0.01, and ****p* < 0.001 by paired two-tailed *t* test. Data are presented as the mean \pm SD. See also Figure S5.



(legend on next page)

upregulated genes, such as *Rgs13* and *Ccnj* (Figure 2G), were significantly upregulated by iMEK treatment and downregulated by IFN- γ treatment, indicating that age-dependent upregulation of some tuft cell-specific genes is induced by other factors (Figure 5Q). In summary, our findings reveal that the combination and the optimal balance of IFN- γ signaling and ERK/MAPK signaling activities preserves the stem cell pool, but these signaling alterations occur at the expense of aging-related changes in enterocytes, enteroendocrine cells, and goblet cells.

Myc is a key regulator of active and quiescent states in intestinal organoids downstream of IFN- γ and ERK/MAPK signaling pathways

To investigate the molecular mechanisms underlying the cross-talk between IFN- γ and ERK/MAPK signaling pathways, we performed bulk RNA-seq on intestinal organoids treated with IFN- γ and/or iMEK for 1, 6, and 24 h. Hierarchical clustering analysis showed that samples treated with IFN- γ or iMEK for 6 or 24 h were grouped into different clusters (Figure 6A). Notably, samples treated with the combination of IFN- γ and iMEK clustered with the IFN- γ -treated samples, indicating that iMEK-induced changes are canceled by IFN- γ treatment at 6 and 24 h.

Then, we examined the effects of IFN- γ treatment on iMEK-treated intestinal organoids (Figures 6B and S6A; Table S5). Among the iMEK-dependent upregulated genes, a small fraction was further upregulated by IFN- γ treatment (group 1), which was associated with immune system processes. In approximately 70% of the iMEK-dependent upregulated genes, IFN- γ treatment suppressed the iMEK-induced upregulation by more than 50% (group 2). GO analysis revealed that antimicrobial peptides were enriched in group 2 at 24 h, therefore indicating the likely differentiation toward the Paneth cell lineage, which is the primary producer of antimicrobial peptides. Therefore, this suggests that iMEK promotes Paneth cell differentiation, whereas IFN- γ treatment reverses these effects. Upstream regulator analysis using IPA software predicted that the activation of several signaling pathways, such as immune response (triggered by lipopolysaccharide), Wnt/ β -catenin signaling (activation of CTNNB1 and TCF7L2), PI3K signaling (inactivation of PI3K inhibitor LY294002), and transforming growth factor- β (TGF- β) signaling (activation of TGFB1), could contribute to iMEK-depen-

dent gene upregulation (Figures 6C and S6B). Among these pathways, Wnt/ β -catenin signaling and TGF- β signaling were inferred to be inactivated by IFN- γ , thereby counteracting the effects induced by iMEK. These results align with the observation that iMEK and IFN- γ tend to have opposing effects on the expression levels of well-known ISC markers regulated by the Wnt/ β -catenin signaling pathway (Figure 6D).

As for iMEK-dependent downregulated genes, in approximately 60% of these genes, IFN- γ treatment prevented this downregulation by more than 50% (Figures 6B and S6A, group 3). Several cell-cycle regulators, such as *Myc*, *E2f1*, and *Ccnd1*, were predicted to regulate group 3 genes (Figures 6E and S6C; Table S6), and their expression levels were also altered by iMEK and/or IFN- γ treatment (Figures 6F and S6D). *E2f1* and *Ccnd1* were downregulated by iMEK, and this effect was blocked by addition of IFN- γ treatment after 6 h. In contrast, *Myc* expression responded as early as 1 h after treatment. Interestingly, IFN- γ treatment alone tended to increase *Myc* expression at an early point, suggesting that *Myc* may be a common downstream target of both the ERK/MAPK and the IFN- γ signaling pathways. Indeed, EdU incorporation analysis showed that inhibiting *Myc* activation with the small-molecule inhibitor 10058-F4 partially reduced the rescue effects of IFN- γ treatment on iMEK-induced quiescence (Figure 6G).

Next, we examined the effects of iMEK on IFN- γ -treated intestinal organoids (Figures 6H and S6E). Among the IFN- γ -dependent upregulated genes, only a small fraction was further upregulated (group 5) or counteracted (group 6) upon iMEK treatment, indicating that IFN- γ -induced genes were largely unaffected by ERK/MAPK signaling. Interestingly, however, MHC class II genes (*H2-Eb1*, *H2-DMA*, *H2-Aa*, and *H2-Ab1*) were among the genes that were synergistically upregulated at 24 h (group 5), suggesting that upregulation of MHC class II gene expression is synergistically regulated by IFN- γ signaling activation and ERK/MAPK signaling inactivation. Among the IFN- γ -dependent downregulated genes, only a small fraction of genes was further downregulated by iMEK (group 8). In approximately 40% of the IFN- γ -dependent downregulated genes, additional iMEK treatment prevented the IFN- γ -induced downregulation by more than 50% (group 7), suggesting that IFN- γ -dependent downregulation is partially counteracted by ERK/MAPK inactivation.

Figure 6. Bulk RNA-seq analysis reveals the combined effects of IFN- γ and iMEK treatment on intestinal organoids

(A) Hierarchical clustering of intestinal organoid samples treated with IFN- γ (1.5 ng/mL) and/or iMEK (3 μ M) for 1, 6, and 24 h. For each condition, two replicates were analyzed.

(B) iMEK-dependent upregulated and downregulated genes at 24 h were classified into four groups (groups 1–4). Grouping criteria are shown on the left. A heatmap representing the genes in each group (center). Representative GO terms enriched in each group (right).

(C) Results of IPA for iMEK-dependent upregulated genes at 24 h (left) and group 2 genes (right). The top five activated or inactivated regulators are listed.

(D) Heatmap showing well-known ISC marker genes at 24 h after treatment.

(E) Results of IPA for iMEK-dependent downregulated genes at 24 h (left) and group 3 genes (right). The top five activated or inactivated regulators are listed.

(F) RT-qPCR analysis of *Myc* ($n = 3$ for 0 h Ctrl, $n = 4$ for other conditions).

(G) PD0325901 (3 μ M) and/or IFN- γ (1.5 ng/mL) was added to the organoid culture medium for 24 h. The *Myc* inhibitor 10058-F4 (50 μ M) was added to the organoids treated with PD0325901 and IFN- γ . EdU (final 10 μ M) was added to the culture medium for the last 2 h of incubation. Representative images of EdU-stained intestinal organoids (top). Scale bars, 100 μ m. The number of EdU-positive cells per circumference (μ m) of organoids from three independent experiments (bottom).

(H) IFN- γ -dependent up-/downregulated genes at 24 h were classified into four groups (groups 5–8). Grouping criteria are shown on the left. A heatmap representing genes in each group (center). Representative GO terms enriched in each group (right).

(F and G) * $p < 0.05$, ** $p < 0.01$, and *** $p < 0.001$ by paired two-tailed t test. Data are presented as the mean \pm SD. See also Figure S6 and Tables S5 and S6.

Collectively, our findings in intestinal organoids demonstrate that global transcriptional changes resulting from the inactivation of ERK/MAPK signaling can largely be counteracted by IFN- γ signaling activation. In addition, we also show Myc transcription factor as a key regulator in shifting between the active and the quiescent states of intestinal organoids downstream of IFN- γ and ERK/MAPK signaling pathways. Moreover, we show that inactivation of ERK/MAPK signaling does not affect IFN- γ -induced gene upregulation or even enhanced IFN- γ -induced MHC class II gene expression. These findings are consistent with our observations in aged ISCs, where immune-response genes activated by IFN- γ signaling are prominently upregulated with age, while cell proliferation states remain unchanged in the ISC population.

The equilibrium between the active and the quiescent states in the aged ISC population

Next, we explored the possibility of an equilibrium existing between the active and the quiescent states in the aged ISC population. Using our scRNA-seq data, we examined the correlation between cell-cycle state and a total of 15 age-dependent upregulated genes, which are the commonly upregulated genes across three studies, including our study, Omrani et al.,¹⁸ and Funk et al.²⁶ (Figures S2E and S7A). Cell-cycle scores in the aged ISC population (cells within the stem cell cluster shown in Figures 2A and 2B) showed only weak correlations ($-0.3 < r < 0.4$) with the expression levels of all individual age-dependent upregulated genes, suggesting that these genes are not strongly associated with cell-cycle state individually. As our organoid data indicated that the balance between IFN- γ and ERK/MAPK signaling is crucial for regulating cell-cycle state, we next investigated whether the balance in expression levels between the downstream genes of IFN- γ and ERK/MAPK signaling—*H2-Aa* and *Ceacam10*, respectively—is associated with cell-cycle state. Indeed, we observed that the balance of *H2-Aa* and *Ceacam10* expression is closely related to cell cycle and cell-type signature (Figures 7A–7C). Aged ISCs with *H2-Aa*-biased expression exhibited high proliferative signatures, indicating that these cells are in the active cycling state (Figures 7A, S7B, and S7C). On the other hand, ISCs with *Ceacam10*-biased expression showed low proliferative and higher stem cell signatures, suggesting that these ISCs are reminiscent of the quiescent Lgr5⁺ ISCs induced by ERK/MAPK inactivation *in vitro* (Figures 7A and 7B, S7C, and S7D). Notably, a fraction of *Ceacam10*-biased ISCs showed an enhanced enteroendocrine cell signature (Figures 7C and S7E), consistent with previous studies showing that quiescent, label-retaining Lgr5⁺ ISCs are precursors of the enteroendocrine cell lineage.^{21,35,36} Thus, our results imply that the balance of *H2-Aa* and *Ceacam10* expression levels is associated with the active and quiescent states of Lgr5⁺ ISCs.

Finally, we investigated how the balance of *H2-Aa* and *Ceacam10* is affected throughout the lifespan *in vivo* (Figure 7D). We observed cooperative changes in intestinal crypt cells over the lifespan, with increased expression of *Ceacam10* and *H2-Aa* in super-aged (28–30 months of age) mice than in middle-aged (12–18 months of age) or aged mice. Our findings underscore a sophisticated balance of intestinal aging marker

expression levels at the individual level. Taken together with our scRNA-seq analysis, which shows that the appropriate balance of aging markers is associated with the optimal balance between active and quiescent states of Lgr5⁺ ISCs, our findings suggest that the synergistic regulation of these aging markers is closely related to the lifelong maintenance of the ISC pool.

DISCUSSION

In this study, we describe an aging-induced signaling mechanism, which is dependent on the synchronized activation of IFN- γ and inactivation of ERK/MAPK signaling pathways, that functions to maintain an equilibrium between active and quiescent states of Lgr5⁺ ISCs during aging. Intriguingly, although each signaling pathway change alone induces severe damage to the intestinal epithelium,^{18–22} the combination of these two pathway changes appears to act as a buffering system to mitigate the deterioration of ISC homeostasis during aging.

Our findings demonstrate that the ISC numbers and proliferative cell state are determined by the balance of activity between the IFN- γ signaling and the ERK/MAPK signaling pathways. In our experiments, aged mice tended to show moderately increased ISC numbers and decreased proliferative capacity in progenitor cells, which suggests that changes in ERK/MAPK signaling have a more significant impact on intestinal homeostasis than changes in IFN- γ signaling. However, whether the ISC number increases, decreases, or is unchanged upon aging remains rather controversial.^{11–16,18,26} At least in part, animal breeding conditions may affect the balance between these two signaling pathways.

Our analysis using intestinal organoids showed that aging-related changes were induced in differentiated cells, especially in enterocytes as well as enteroendocrine and goblet cells, under combined treatment with iMEK and IFN- γ . These results are consistent with our *in vivo* observations that the differentiated cell types represented more prominent aging-induced changes than ISCs. Interestingly, genes involved in lipid transport and metabolism were upregulated in aged mature enterocytes, suggesting that the changes in enterocyte maturation may be associated with lipid metabolism disorders. Previous studies have shown that an increase in enteroendocrine cells induces enhanced lipid metabolism and impaired glucose homeostasis.^{37,38} Our findings support the possibility that aging-related changes in these two cell types may affect the metabolism of the whole body and induce aging-related diseases in other organs. Furthermore, one of the age-dependent goblet cell-specific downregulated genes, *Clca1*, has been reported to regulate mucus barrier function,^{39,40} indicating that aging-related changes in goblet cells may impair the mucus barrier functions, leading to systemic inflammation. Therefore, resetting both ERK/MAPK and IFN- γ signaling activities to a younger state may have beneficial effects as a potential antiaging therapeutic strategy, with a minimum impact on ISCs.

Microbiome dysbiosis and immune cell activation are often observed in the aged intestine,^{9,10} suggesting that the tissue microenvironment modulates ERK/MAPK and IFN- γ signaling pathways. Our analysis showed that the activation of the

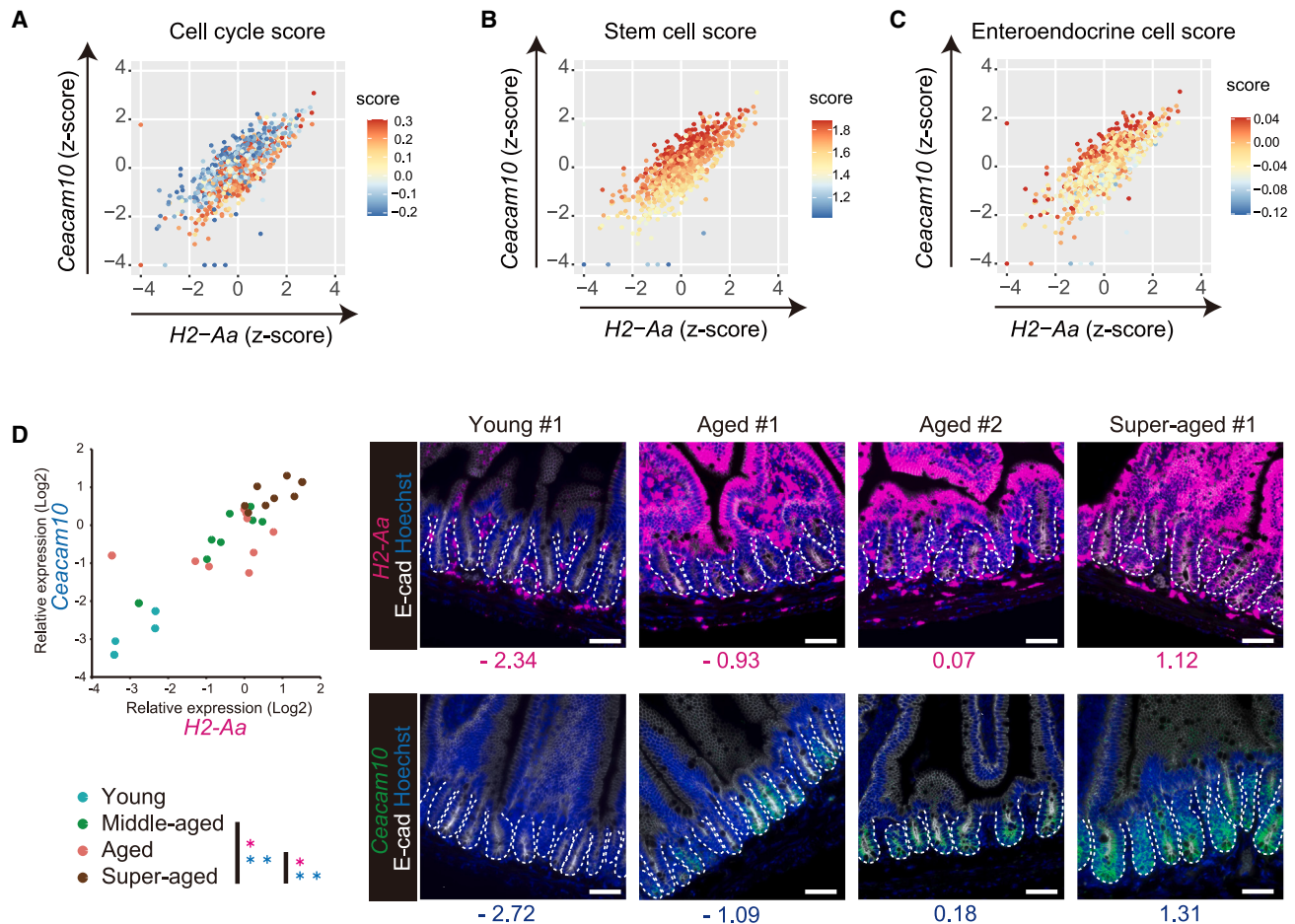


Figure 7. The balance of aging markers is associated with the active and quiescent states of aged ISCs

(A–C) Scatterplots of aging markers in aged mouse-derived ISCs using our scRNA-seq data. The expression levels of *H2-Aa* and *Ceacam10* are shown in the Z score using aged mouse-derived ISCs (cells in stem cell cluster). The cell cycle score, stem cell score, and enteroendocrine cell score for each cell are shown in the indicated colors.

(D) Scatterplot of *H2-Aa* and *Ceacam10* expression levels in intestinal crypt cells from young male (2 months of age, $n = 4$), middle-aged male (12–18 months of age, $n = 7$), aged male (24–27 months of age, $n = 9$), and super-aged male (28–30 months of age, $n = 9$) mice (left). Expression levels were analyzed by RNA *in situ* hybridization, and the relative signal intensity in the crypt area is shown. The statistical results for *H2-Aa* expression are shown in pink, and *Ceacam10* expression is shown in blue. * $p < 0.05$ and ** $p < 0.01$ by two-tailed Welch's t test. Representative images of *H2-Aa* and *Ceacam10* RNA *in situ* hybridization (right). Images in the same column are from the same mouse intestine sample. Scale bars, 50 μ m.

See also Figure S7.

TLR1/2 signaling pathway can also induce *Ceacam10* expression (Figure 4D). Moreover, previous studies have shown that *Tlr1* or *Tlr2* knockout in young mice increases cell proliferation and decreases enteroendocrine cell numbers in the colon,^{41,42} which are opposite effects to those observed in the aged intestine. Therefore, ERK/MAPK signaling inactivation may be related to gut microbiota-induced TLR1/2 signaling activation, although further investigation is necessary. Our transcriptome analysis showed that IFNs are not expressed in any of the intestinal epithelial cell types. A recent report has shown that the cytotoxic CD4 T cells and group 2 innate lymphoid (ILC2) cells in the intestinal lamina propria express IFN- γ in aged mice.¹⁸ Our data also showed increased infiltration of CD4 T cells in the area surrounding the crypts (Figure 1D), indicating that CD4 T cell-derived IFN- γ may affect aged ISCs. Interest-

ingly, our bulk RNA-seq analysis of intestinal organoids revealed that IFN- γ -induced MHC class II gene expression was further enhanced by iMEK (Figure 6H). These findings suggest the potential presence of a signaling buffering system mediated by cell-cell interaction between ISCs and CD4 T cells, in which ERK/MAPK signaling inactivation enhances MHC class II expression in ISCs, thereby recruiting more CD4 T cells to ISCs through T cell receptor (TCR)-MHC interactions and amplifying the activation of IFN- γ signaling in ISCs. Further analyses of the gut microbiome and immune cells would be necessary to clarify the process of intestinal epithelial aging.

In summary, our study identifies the network of signaling pathways necessary for maintenance of the ISC pool during aging and clarifies the importance of studying the combinational

effects and the balance of multiple signaling pathways during organ aging, which will provide new potential avenues for better antiaging therapeutic strategies.

Limitations of the study

Our data indicate that modulating IFN- γ and ERK/MAPK signaling pathways in intestinal organoids partially mimics the aging process of the intestinal epithelium. However, the *in vivo* aging process involves various additional changes. Since ERK/MAPK activation occurs in a pulse-like pattern *in vivo*,³⁴ more precise temporal modulation of ERK/MAPK signaling may be essential to more accurately recapitulate the aging process. Furthermore, the effects of upstream regulators of *Ly6e* on intestinal organoids were not examined in this study, and hence, future studies could explore the modulation of multiple signaling pathways in intestinal organoids to advance an *ex vivo* model of intestinal epithelium aging.

In this study, we demonstrate that the equilibrium between active and quiescent states of Lgr5⁺ ISCs is associated with the balance between IFN- γ and ERK/MAPK signaling pathways. While previous studies using young mice have identified quiescent, injury-inducible “reserve stem cells” or “+4 cells” with properties distinct from those of Lgr5⁺ ISCs,⁴³ our study did not analyze the dynamics of these quiescent, reserve stem cells/+4 cells during aging.

In this study, aging-related changes in gene expression were more pronounced in male mice, with a notable increase in the expression of MHC class II genes observed specifically in males. Consequently, the experiments presented from Figure 2 onward primarily utilized male mice. The potential sex-specific difference in the balance between the IFN- γ signaling pathway and the ERK/MAPK signaling pathway remains an open question for future investigation.

RESOURCE AVAILABILITY

Lead contact

Requests for further information and resources and reagents should be directed to and will be fulfilled by the lead contact, Takuya Yamamoto (takuya@cira.kyoto-u.ac.jp).

Materials availability

This study did not generate new materials or unique reagents.

Data and code availability

- Sequencing data have been deposited with Gene Expression Omnibus (GEO) and are publicly available as of the date of publication. Accession numbers are listed in the [key resources table](#).
- This paper does not report original code.
- Any additional information required to reanalyze the data reported in this paper is available from the [lead contact](#) upon request.

ACKNOWLEDGMENTS

We thank the members of our laboratory and CiRA for their valuable scientific discussions and administrative support. We thank Dr. K. Mitsunaga, K. Okita, T. Iseki, Y. Zhang, K. Deguchi, E. Kawaguchi, and J. Asahira for their technical assistance; Dr. M. Imajo for technical advice on intestine experiments; Dr. M. Kusakabe, Dr. A. Kakizuka, and Dr. Y. Oda for conventional animal facilities; the Center for Anatomical, Pathological and Forensic Medical Research, Kyoto University Graduate School of Medicine, for preparing microscopy slides; the

Single-Cell Genome Information Analysis Core (SignAC) in ASHBi for RNA sequencing; and Dr. S. Goulas for reviewing the manuscript. The graphical abstract was created by BioRender.com. This work was supported in part by AMED-CREST JP18gm0610017 (to E.N. and T.Y.); AMED-CREST JP17gm1110004, JP19gm1310002, and JP21gm1310011 (to T.Y.); AMED, the Core Center for iPS Cell Research, JP22bm0104001 (to T.Y.); JSPS A3 Foresight Program JPJSA3F20230001 (to T.Y.); JST FOREST Program JPMJFR206C (to T.Y.); JST, CREST, JPMJCR2023 (to T.Y.); JSPS KAKENHI 20K16143 and 24K18422 (to M.N.-K.); the iPS Cell Research Fund (to T.Y. and M.N.-K.); a Grant-in-Aid for JSPS RPD research fellowship (to M.N.-K.); and a iPS Academia Japan research grant (to M.N.-K.).

AUTHOR CONTRIBUTIONS

Conceptualization, M.N.-K. and T.Y.; methodology, M.N.-K.; investigation, M.N.-K., J.L., Y.S., A.H., and M. Kimura; data analysis, M.N.-K., M. Kabata, S.S., and T.Y.; SC3-seq technologies, T.N. and M.S.; support for scRNA-seq data analysis, Y.I. and Y. Hiraoka; experimental support, K.K. and Y. Hamazaki; writing – original draft, M.N.-K. and T.Y.; writing – review & editing, M.N.-K., E.N., and T.Y.; funding acquisition, M.N.-K., E.N., and T.Y.; supervision, E.N. and T.Y.

DECLARATION OF INTERESTS

The authors declare no competing interests.

STAR★METHODS

Detailed methods are provided in the online version of this paper and include the following:

- [KEY RESOURCES TABLE](#)
- [EXPERIMENTAL MODEL AND STUDY PARTICIPANT DETAILS](#)
 - Mouse husbandry
 - Small intestinal organoid culture
- [METHOD DETAILS](#)
 - 5-FU injection to mice
 - EdU injection to mice
 - Tissue sample preparation and phenotypic analysis
 - Flow cytometry
 - RNA *in situ* hybridization
 - Intestinal organoid treatments
 - RT-qPCR
 - Library preparation for bulk population RNA-seq in [Figure 1](#)
 - Bulk population RNA-seq data analyses in [Figure 1](#)
 - Library preparation for single-cell RNA-seq
 - Analysis of the scRNA-seq data
 - Integrative analysis of the three scRNA-seq datasets
 - Library preparation for bulk population RNA-seq in [Figure 6](#)
 - Bulk population RNA-seq data analyses in [Figure 6](#)
 - Data availability
- [QUANTIFICATION AND STATISTICAL ANALYSIS](#)

SUPPLEMENTAL INFORMATION

Supplemental information can be found online at <https://doi.org/10.1016/j.celrep.2025.115286>.

Received: March 7, 2024

Revised: December 9, 2024

Accepted: January 17, 2025

Published: February 13, 2025

REFERENCES

1. Barker, N., van Es, J.H., Kuipers, J., Kujala, P., van den Born, M., Cozijnsen, M., Haegebarth, A., Korving, J., Begthel, H., Peters, P.J., and Clevers,

- H. (2007). Identification of stem cells in small intestine and colon by marker gene *Lgr5*. *Nature* 449, 1003–1007. <https://doi.org/10.1038/nature06196>.
2. Beumer, J., and Clevers, H. (2021). Cell fate specification and differentiation in the adult mammalian intestine. *Nat. Rev. Mol. Cell Biol.* 22, 39–53. <https://doi.org/10.1038/s41580-020-0278-0>.
3. Sato, T., Vries, R.G., Snippert, H.J., van de Wetering, M., Barker, N., Stange, D.E., van Es, J.H., Abo, A., Kujala, P., Peters, P.J., and Clevers, H. (2009). Single *Lgr5* stem cells build crypt-villus structures in vitro without a mesenchymal niche. *Nature* 459, 262–265. <https://doi.org/10.1038/nature07935>.
4. Gregorieff, A., Pinto, D., Begthel, H., Destrée, O., Kielman, M., and Clevers, H. (2005). Expression pattern of Wnt signaling components in the adult intestine. *Gastroenterology* 129, 626–638. <https://doi.org/10.1053/j.gastro.2005.06.007>.
5. Shoshkes-Carmel, M., Wang, Y.J., Wangenstein, K.J., Tóth, B., Kondo, A., Massasa, E.E., Itzkovitz, S., and Kaestner, K.H. (2018). Subepithelial telocytes are an important source of Wnts that supports intestinal crypts. *Nature* 557, 242–246. <https://doi.org/10.1038/s41586-018-0084-4>.
6. Sato, T., van Es, J.H., Snippert, H.J., Stange, D.E., Vries, R.G., van den Born, M., Barker, N., Shroyer, N.F., van de Wetering, M., and Clevers, H. (2011). Paneth cells constitute the niche for *Lgr5* stem cells in intestinal crypts. *Nature* 469, 415–418. <https://doi.org/10.1038/nature09637>.
7. McCarthy, N., Manieri, E., Storm, E.E., Saadatpour, A., Luoma, A.M., Kapoor, V.N., Madha, S., Gaynor, L.T., Cox, C., Keerthivasan, S., et al. (2020). Distinct Mesenchymal Cell Populations Generate the Essential Intestinal BMP Signaling Gradient. *Cell Stem Cell* 26, 391–402.e5. <https://doi.org/10.1016/j.stem.2020.01.008>.
8. Biton, M., Haber, A.L., Rogel, N., Burgin, G., Beyaz, S., Schnell, A., Ashenberg, O., Su, C.W., Smillie, C., Shekhar, K., et al. (2018). T Helper Cell Cytokines Modulate Intestinal Stem Cell Renewal and Differentiation. *Cell* 175, 1307–1320.e22. <https://doi.org/10.1016/j.cell.2018.10.008>.
9. Thevaranjan, N., Puchta, A., Schulz, C., Naidoo, A., Szamosi, J.C., Verschoor, C.P., Loukov, D., Schenck, L.P., Jury, J., Foley, K.P., et al. (2017). Age-Associated Microbial Dysbiosis Promotes Intestinal Permeability, Systemic Inflammation, and Macrophage Dysfunction. *Cell Host Microbe* 21, 455–466.e4. <https://doi.org/10.1016/j.chom.2017.03.002>.
10. Sovran, B., Hugenholtz, F., Elderman, M., Van Beek, A.A., Gravensen, K., Huijskes, M., Boekschoten, M.V., Savelkoul, H.F.J., De Vos, P., Dekker, J., and Wells, J.M. (2019). Age-associated impairment of the Mucus Barrier Function is Associated with Profound Changes in Microbiota and Immunity. *Sci. Rep.* 9, 1437. <https://doi.org/10.1038/s41598-018-35228-3>.
11. Nalapareddy, K., Nattamai, K.J., Kumar, R.S., Karns, R., Wikenheiser-Bronk, K.A., Sampson, L.L., Mahe, M.M., Sundaram, N., Yacyshyn, M.B., Yacyshyn, B., et al. (2017). Canonical Wnt Signaling Ameliorates Aging of Intestinal Stem Cells. *Cell Rep.* 18, 2608–2621. <https://doi.org/10.1016/j.celrep.2017.02.056>.
12. Moorefield, E.C., Andres, S.F., Blue, R.E., Van Landeghem, L., Mah, A.T., Santoro, M.A., and Ding, S. (2017). Aging effects on intestinal homeostasis associated with expansion and dysfunction of intestinal epithelial stem cells. *Aging-Us* 9, 1898–1915. <https://doi.org/10.18632/aging.101279>.
13. Mihaylova, M.M., Cheng, C.W., Cao, A.Q., Tripathi, S., Mana, M.D., Bauer-Rowe, K.E., Abu-Remaih, M., Clavaun, L., Erdemir, A., Lewis, C.A., et al. (2018). Fasting Activates Fatty Acid Oxidation to Enhance Intestinal Stem Cell Function during Homeostasis and Aging. *Cell Stem Cell* 22, 769–778.e4. <https://doi.org/10.1016/j.stem.2018.04.001>.
14. Igarashi, M., Miura, M., Williams, E., Jaksch, F., Kadowaki, T., Yamauchi, T., and Guarente, L. (2019). NAD(+) supplementation rejuvenates aged gut adult stem cells. *Aging Cell* 18, e12935. <https://doi.org/10.1111/accel.12935>.
15. He, D., Wu, H., Xiang, J., Ruan, X., Peng, P., Ruan, Y., Chen, Y.G., Wang, Y., Yu, Q., Zhang, H., et al. (2020). Gut stem cell aging is driven by mTORC1 via a p38 MAPK-p53 pathway. *Nat. Commun.* 11, 37. <https://doi.org/10.1038/s41467-019-13911-x>.
16. Pentimikko, N., Iqbal, S., Mana, M., Andersson, S., Cognetta, A.B., Suci, R.M., Roper, J., Luopajarvi, K., Markelin, E., Gopalakrishnan, S., et al. (2019). Notum produced by Paneth cells attenuates regeneration of aged intestinal epithelium. *Nature* 571, 398–402. <https://doi.org/10.1038/s41586-019-1383-0>.
17. Nefzger, C.M., Jardé, T., Srivastava, A., Schroeder, J., Rossello, F.J., Horvay, K., Prasko, M., Paynter, J.M., Chen, J., Weng, C.F., et al. (2022). Intestinal stem cell aging signature reveals a reprogramming strategy to enhance regenerative potential. *NPJ Regen. Med.* 7, 31. <https://doi.org/10.1038/s41536-022-00226-7>.
18. Omrani, O., Krepelova, A., Rasa, S.M.M., Sirvinskas, D., Lu, J., Annunziata, F., Garside, G., Bajwa, S., Reinhardt, S., Adam, L., et al. (2023). IFN γ -Stat1 axis drives aging-associated loss of intestinal tissue homeostasis and regeneration. *Nat. Commun.* 14, 6109. <https://doi.org/10.1038/s41467-023-41683-y>.
19. Eriguchi, Y., Nakamura, K., Yokoi, Y., Sugimoto, R., Takahashi, S., Hashimoto, D., Teshima, T., Ayabe, T., Selsted, M.E., and Ouellette, A.J. (2018). Essential role of IFN-gamma in T cell-associated intestinal inflammation. *Jci Insight* 3, e121886. <https://doi.org/10.1172/jci.insight.121886>.
20. Takashima, S., Martin, M.L., Jansen, S.A., Fu, Y., Bos, J., Chandra, D., O'Connor, M.H., Mertelsmann, A.M., Vinci, P., Kuttiyara, J., et al. (2019). T cell-derived interferon-gamma programs stem cell death in immune-mediated intestinal damage. *Sci. Immunol.* 4, eaay8556. <https://doi.org/10.1126/sciimmunol.aay8556>.
21. Basak, O., Beumer, J., Wiebrands, K., Seno, H., van Oudenaarden, A., and Clevers, H. (2017). Induced Quiescence of *Lgr5*+Stem Cells in Intestinal Organoids Enables Differentiation of Hormone-Producing Enteroendocrine Cells. *Cell Stem Cell* 20, 177–190.e4. <https://doi.org/10.1016/j.stem.2016.11.001>.
22. de Jong, P.R., Taniguchi, K., Harris, A.R., Bertin, S., Takahashi, N., Duong, J., Campos, A.D., Powis, G., Corr, M., Karin, M., and Raz, E. (2016). ERK5 signalling rescues intestinal epithelial turnover and tumour cell proliferation upon ERK1/2 abrogation. *Nat. Commun.* 7, 11551. <https://doi.org/10.1038/ncomms11551>.
23. Van der Flier, L.G., Haegebarth, A., Stange, D.E., Van de Wetering, M., and Clevers, H. (2009). OLFM4 Is a Robust Marker for Stem Cells in Human Intestine and Marks a Subset of Colorectal Cancer Cells. *Gastroenterology* 137, 15–17. <https://doi.org/10.1053/j.gastro.2009.05.035>.
24. Haber, A.L., Biton, M., Rogel, N., Herbst, R.H., Shekhar, K., Smillie, C., Burgin, G., Delorey, T.M., Howitt, M.R., Katz, Y., et al. (2017). A single-cell survey of the small intestinal epithelium. *Nature* 551, 333–339. <https://doi.org/10.1038/nature24489>.
25. Moor, A.E., Harnik, Y., Ben-Moshe, S., Massasa, E.E., Rozenberg, M., Eilam, R., Bahar Halpern, K., and Itzkovitz, S. (2018). Spatial Reconstruction of Single Enterocytes Unveils Broad Zonation along the Intestinal Villus Axis. *Cell* 175, 1156–1167.e15. <https://doi.org/10.1016/j.cell.2018.08.063>.
26. Funk, M.C., Gleixner, J.G., Heigwer, F., Vonficht, D., Valentini, E., Aydin, Z., Tonin, E., Del Prete, S., Mahara, S., Throm, Y., et al. (2023). Aged intestinal stem cells propagate cell-intrinsic sources of inflammaging in mice. *Dev. Cell* 58, 2914–2929.e7. <https://doi.org/10.1016/j.devcel.2023.11.013>.
27. Gebert, N., Cheng, C.W., Kirkpatrick, J.M., Di Fraia, D., Yun, J., Schädel, P., Pace, S., Garside, G.B., Werz, O., Rudolph, K.L., et al. (2020). Region-Specific Proteome Changes of the Intestinal Epithelium during Aging and Dietary Restriction. *Cell Rep.* 31, 107565. <https://doi.org/10.1016/j.celrep.2020.107565>.
28. Thelemann, C., Eren, R.O., Coutaz, M., Brasseit, J., Bouzourene, H., Rosa, M., Duval, A., Lavanchy, C., Mack, V., Mueller, C., et al. (2014). Interferon-gamma Induces Expression of MHC Class II on Intestinal Epithelial Cells and Protects Mice from Colitis. *PLoS One* 9, e86844. <https://doi.org/10.1371/journal.pone.0086844>.
29. Koyama, M., Mukhopadhyay, P., Schuster, I.S., Henden, A.S., Hülsdünker, J., Varelias, A., Vetzizou, M., Kuns, R.D., Robb, R.J., Zhang, P., et al. (2019). MHC Class II Antigen Presentation by the Intestinal

- Epithelium Initiates Graft-versus-Host Disease and Is Influenced by the Microbiota. *Immunity* 51, 885–898.e7. <https://doi.org/10.1016/j.immuni.2019.08.011>.
30. Mar, K.B., Rinkenberger, N.R., Boys, I.N., Eitson, J.L., McDougal, M.B., Richardson, R.B., and Schoggins, J.W. (2018). LY6E mediates an evolutionarily conserved enhancement of virus infection by targeting a late entry step. *Nat. Commun.* 9, 3603. <https://doi.org/10.1038/s41467-018-06000-y>.
 31. Xu, X., Qiu, C., Zhu, L., Huang, J., Li, L., Fu, W., Zhang, L., Wei, J., Wang, Y., Geng, Y., et al. (2014). IFN-Stimulated Gene LY6E in Monocytes Regulates the CD14/TLR4 Pathway but Inadequately Restrains the Hyperactivation of Monocytes during Chronic HIV-1 Infection. *J. Immunol.* 193, 4125–4136. <https://doi.org/10.4049/jimmunol.1401249>.
 32. Platanias, L.C. (2005). Mechanisms of type-I- and type-II-interferon-mediated signalling. *Nat. Rev. Immunol.* 5, 375–386. <https://doi.org/10.1038/nri1604>.
 33. Mesev, E.V., LeDesma, R.A., and Ploss, A. (2019). Decoding type I and III interferon signalling during viral infection. *Nat. Microbiol.* 4, 914–924. <https://doi.org/10.1038/s41564-019-0421-x>.
 34. Muta, Y., Fujita, Y., Sumiyama, K., Sakurai, A., Taketo, M.M., Chiba, T., Seno, H., Aoki, K., Matsuda, M., and Imajo, M. (2018). Composite regulation of ERK activity dynamics underlying tumour-specific traits in the intestine. *Nat. Commun.* 9, 2174. <https://doi.org/10.1038/s41467-018-04527-8>.
 35. Buczaccki, S.J.A., Zecchini, H.I., Nicholson, A.M., Russell, R., Vermeulen, L., Kemp, R., and Winton, D.J. (2013). Intestinal label-retaining cells are secretory precursors expressing Lgr5. *Nature* 495, 65–69. <https://doi.org/10.1038/nature11965>.
 36. Yan, K.S., Gevaert, O., Zheng, G.X.Y., Anchang, B., Probert, C.S., Larkin, K.A., Davies, P.S., Cheng, Z.F., Kaddis, J.S., Han, A., et al. (2017). Intestinal Enterendocrine Lineage Cells Possess Homeostatic and Injury-Inducible Stem Cell Activity. *Cell Stem Cell* 21, 78–90.e6. <https://doi.org/10.1016/j.stem.2017.06.014>.
 37. Mellitzer, G., Beucher, A., Lobstein, V., Michel, P., Robine, S., Kedinger, M., and Gradwohl, G. (2010). Loss of enteroendocrine cells in mice alters lipid absorption and glucose homeostasis and impairs postnatal survival. *J. Clin. Invest.* 120, 1708–1721. <https://doi.org/10.1172/jci40794>.
 38. Martin, A.M., Yabut, J.M., Choo, J.M., Page, A.J., Sun, E.W., Jessup, C.F., Wesselingh, S.L., Khan, W.I., Rogers, G.B., Steinberg, G.R., and Keating, D.J. (2019). The gut microbiome regulates host glucose homeostasis via peripheral serotonin. *Proc. Natl. Acad. Sci. USA* 116, 19802–19804. <https://doi.org/10.1073/pnas.1909311116>.
 39. Nyström, E.E.L., Birchenough, G.M.H., van der Post, S., Arike, L., Gruber, A.D., Hansson, G.C., and Johansson, M.E.V. (2018). Calcium-activated Chloride Channel Regulator 1 (CLCA1) Controls Mucus Expansion in Colon by Proteolytic Activity. *EBioMedicine* 33, 134–143. <https://doi.org/10.1016/j.ebiom.2018.05.031>.
 40. Nyström, E.E.L., Arike, L., Ehrencrona, E., Hansson, G.C., and Johansson, M.E.V. (2019). Calcium-activated chloride channel regulator 1 (CLCA1) forms non-covalent oligomers in colonic mucus and has mucin 2-processing properties. *J. Biol. Chem.* 294, 17075–17089. <https://doi.org/10.1074/jbc.RA119.009940>.
 41. Kamdar, K., Johnson, A.M.F., Chac, D., Myers, K., Kulur, V., Truevillian, K., and DePaolo, R.W. (2018). Innate Recognition of the Microbiota by TLR1 Promotes Epithelial Homeostasis and Prevents Chronic Inflammation. *J. Immunol.* 201, 230–242. <https://doi.org/10.4049/jimmunol.1701216>.
 42. Wang, H., Kwon, Y.H., Dewan, V., Vahedi, F., Syed, S., Fontes, M.E., Ashkar, A.A., Surette, M.G., and Khan, W.I. (2019). TLR2 Plays a Pivotal Role in Mediating Mucosal Serotonin Production in the Gut. *J. Immunol.* 202, 3041–3052. <https://doi.org/10.4049/jimmunol.1801034>.
 43. Bankaitis, E.D., Ha, A., Kuo, C.J., and Magness, S.T. (2018). Reserve Stem Cells in Intestinal Homeostasis and Injury. *Gastroenterology* 155, 1348–1361. <https://doi.org/10.1053/j.gastro.2018.08.016>.
 44. Schneider, C.A., Rasband, W.S., and Eliceiri, K.W. (2012). NIH Image to ImageJ: 25 years of image analysis. *Nat. Methods* 9, 671–675. <https://doi.org/10.1038/nmeth.2089>.
 45. Martin, M. (2011). Cutadapt removes adapter sequences from high-throughput sequencing reads. *EMBnet. j.* 17, 10. <https://doi.org/10.14806/ej.17.1.200>.
 46. Dobin, A., Davis, C.A., Schlesinger, F., Drenkow, J., Zaleski, C., Jha, S., Batut, P., Chaisson, M., and Gingeras, T.R. (2013). STAR: ultrafast universal RNA-seq aligner. *Bioinformatics* 29, 15–21. <https://doi.org/10.1093/bioinformatics/bts635>.
 47. Anders, S., Pyl, P.T., and Huber, W. (2015). HTSeq—a Python framework to work with high-throughput sequencing data. *Bioinformatics* 31, 166–169. <https://doi.org/10.1093/bioinformatics/btu638>.
 48. Love, M.I., Huber, W., and Anders, S. (2014). Moderated estimation of fold change and dispersion for RNA-seq data with DESeq2. *Genome Biol.* 15, 550. <https://doi.org/10.1186/s13059-014-0550-8>.
 49. Huang, D.W., Sherman, B.T., and Lempicki, R.A. (2009). Systematic and integrative analysis of large gene lists using DAVID bioinformatics resources. *Nat. Protoc.* 4, 44–57. <https://doi.org/10.1038/nprot.2008.211>.
 50. Butler, A., Hoffman, P., Smibert, P., Papalexi, E., and Satija, R. (2018). Integrating single-cell transcriptomic data across different conditions, technologies, and species. *Nat. Biotechnol.* 36, 411–420. <https://doi.org/10.1038/nbt.4096>.
 51. Imoto, Y., Nakamura, T., Escobar, E.G., Yoshiwaki, M., Kojima, Y., Yabuta, Y., Katou, Y., Yamamoto, T., Hiraoka, Y., and Saitou, M. (2022). Resolution of the curse of dimensionality in single-cell RNA sequencing data analysis. *Life Sci. Alliance* 5, e202201591. <https://doi.org/10.26508/lsa.202201591>.
 52. Subramanian, A., Tamayo, P., Mootha, V.K., Mukherjee, S., Ebert, B.L., Gillette, M.A., Paulovich, A., Pomeroy, S.L., Golub, T.R., Lander, E.S., and Mesirov, J.P. (2005). Gene set enrichment analysis: a knowledge-based approach for interpreting genome-wide expression profiles. *Proc. Natl. Acad. Sci. USA* 102, 15545–15550. <https://doi.org/10.1073/pnas.0506580102>.
 53. Nakamura, T., Yabuta, Y., Okamoto, I., Aramaki, S., Yokobayashi, S., Kurimoto, K., Sekiguchi, K., Nakagawa, M., Yamamoto, T., and Saitou, M. (2015). SC3-seq: a method for highly parallel and quantitative measurement of single-cell gene expression. *Nucleic Acids Res.* 43, e60. <https://doi.org/10.1093/nar/gkv134>.
 54. Ishikura, Y., Yabuta, Y., Ohta, H., Hayashi, K., Nakamura, T., Okamoto, I., Yamamoto, T., Kurimoto, K., Shirane, K., Sasaki, H., and Saitou, M. (2016). In Vitro Derivation and Propagation of Spermatogonial Stem Cell Activity from Mouse Pluripotent Stem Cells. *Cell Rep.* 17, 2789–2804. <https://doi.org/10.1016/j.celrep.2016.11.026>.
 55. Tirosh, I., Izar, B., Prakadan, S.M., Wadsworth, M.H., Treacy, D., Trombetta, J.J., Rotem, A., Rodman, C., Lian, C., Murphy, G., et al. (2016). Dissecting the multicellular ecosystem of metastatic melanoma by single-cell RNA-seq. *Science* 352, 189–196. <https://doi.org/10.1126/science.aad0501>.

STAR★METHODS

KEY RESOURCES TABLE

REAGENT or RESOURCE	SOURCE	IDENTIFIER
Antibodies		
anti-Ki67	Abcam	Cat# ab15580; RRID:AB_443209
anti-Olfm4	Cell Signaling Technology	Cat# 39141; RRID: AB_2650511
anti-CD4	Abcam	Cat# ab183685; RRID: AB_2686917
anti-Lyz1	Abcam	Cat# ab108508; RRID: AB_10861277
anti-Chromogranin A	Abcam	Cat# ab15160; RRID: AB_301704
anti-Dclk1	Abcam	Cat# ab37994; RRID: AB_873538
anti-phospho-ERK1/2	Cell Signaling Technology	Cat# 4376; RRID: AB_331772
anti-E-Cadherin	BD Biosciences	Cat# 610181; RRID: AB_397580
Histofine Simple Stain Mouse MAX-PO (R)	Nichirei Biosciences	Cat# 414341F; RRID: AB_2819094
Goat anti-Rabbit IgG (H+L) Highly Cross-Adsorbed Secondary Antibody, Alexa Fluor™ 488	Thermo Fisher Scientific	Cat# A-11034; RRID: AB_2576217
Goat anti-Rabbit IgG (H+L) Highly Cross-Adsorbed Secondary Antibody, Alexa Fluor™ 594	Thermo Fisher Scientific	Cat# A-11037; RRID: AB_253409
Goat anti-Mouse IgG (H+L) Cross-Adsorbed Secondary Antibody, Alexa Fluor™ 633	Thermo Fisher Scientific	Cat# A-21050; RRID: AB_2535718
EPCAM-APC(G8.8)	BioLegend	Cat# 118213; RRID: AB_1134105
CD24-Pacific Blue (M1/69)	BioLegend	Cat# 101819; RRID: AB_572010
CD45-PE/Cy7 (30-F11)	BioLegend	Cat# 103113; RRID: AB_312978
Ter119-PE/Cy7 (TER-119)	BioLegend	Cat# 116221; RRID: AB_2137789
CD31-PE/Cy7 (Mec13.3)	BioLegend	Cat# 102523; RRID: AB_2572181
Chemicals, peptides, and recombinant proteins		
5-FU	Sigma–Aldrich	F6627
EdU	Thermo Fisher Scientific	A10044
10 mM Tris-HCl buffer at pH 9.0 containing 1 mM EDTA	Agilent	S2367
10 mM citrate buffer at pH 6.0	Agilent	S1699
ImmPACT DAB	Vector Labs	SK-4105
Alcian blue solution	Nacalai	37154
nuclear fast red	Scytek Laboratories	NFS125
TrypLE Express	Thermo Fisher Scientific	12604013
DNaseI	Roche	4716728001
MEM	Thermo Fisher Scientific	11380037
7-AAD	BD Bioscience	559925
RNase inhibitor	Thermo Fisher Scientific	10777019
Y27632	Tocris Bioscience	1254
Matrigel	Corning	356231
advanced DMEM/F12	Thermo Fisher Scientific	12634
GlutaMax	Thermo Fisher Scientific	35050
HEPES	Thermo Fisher Scientific	15630
N2 supplement	Thermo Fisher Scientific	17502
B27 supplement	Thermo Fisher Scientific	17504
mouse recombinant EGF	R&D Systems	2028

(Continued on next page)

Continued

REAGENT or RESOURCE	SOURCE	IDENTIFIER
mouse recombinant Noggin	PeproTech	250-38
human recombinant R-spondin-1	R&D Systems	4645-RS
<i>N</i> -acetyl-L-cysteine	Sigma-Aldrich	A9165
mouse recombinant IFN- γ	PeproTech	315-05
mouse recombinant IFN- α	BioLegend	752802
mouse recombinant TNF- α	PeproTech	315-01A
Pam3CSK4	InvivoGen	tlrl-pms
Poly (I:C)	Tocris Bioscience	4287
LPS	Sigma-Aldrich	L4391
Retinoic Acid	Sigma-Aldrich	R2625
MHY1485	Sigma-Aldrich	SML0810
EX527	Santa Cruz	sc-203044
PD0325901	Wako	162-25291
Etomoxir	Sigma-Aldrich	E1905
dimethyl sulfoxide	Sigma-Aldrich	D2650
Ruxolitinib	Selleck	S1378
Recombinant Mouse IL-28B/IFN-lambda 3	R&D Systems	1789-ML
SB203580	Merck Millipore	559389
SP600125	Merck Millipore	420119
BAY 11-7082	Selleck	S2913
IWP2	Selleck	S7085
Propidium Iodide	Sigma-Aldrich	P-4170
Cell Recovery Solution	Corning	354253
Critical commercial assays		
Click-iT EdU Alexa Fluor 488 Imaging Kit	Thermo Fisher Scientific	C10337
Vectastain Elite ABC Rabbit IgG kit	Vector Labs	PK-6101
Histofine DAB	Nichirei Biosciences	425011
RNAScope Multiplex Fluorescent v2	Advanced Cell Diagnostics	323100
QIAshredder	Qiagen	79656
RNeasy mini kit	Qiagen	74106
RNeasy micro kit	Qiagen	74004
QuantiTect reverse transcription kit	Qiagen	205311
SYBR Premix Ex TaqII	Takara	RR820
NextSeq 500 High Output v2 Kit	Illumina	FC-404-2005
Single Cell 3' Reagent Kits v3.1	10X Genomics	1000128
Next GEM Chip G Single Cell Kit	10X Genomics	1000127
Illumina Stranded mRNA Prep, Ligation kit	Illumina	20040532
Deposited data		
Bulk population RNA-seq data in Figure 1	This paper	GEO: GSE210242
Single-cell RNA-seq data	This paper	GEO: GSE210242
Bulk population RNA-seq data in Figure 6	This paper	GEO: GSE210242
Experimental models: Cell lines		
Mouse intestinal organoids	This paper	N/A
Experimental models: Organisms/strains		
Lgr5-eGFP-IRES-CreERT2	Jackson	RRID: IMSR_JAX:008875
C57BL/6JmsSlc	Japan SLC	http://www.jslc.co.jp/animals/mouse.php
Oligonucleotides		
Primers used for qRT-PCR, see Table S7	This Study	N/A

(Continued on next page)

Continued

REAGENT or RESOURCE	SOURCE	IDENTIFIER
Oligonucleotides used for SC3-seq method, see Table S7	This Study	N/A
Software and algorithms		
ImageJ	Schneider et al. ⁴⁴	https://imagej.net/ij/
FACSDiva	BD Biosciences	N/A
FACSFlowJo	BD Biosciences	N/A
NIS-Elements AR	Nikon	N/A
GraphPad Prism	GraphPad Software	N/A
Ingenuity Pathway Analysis	Qiagen	N/A
R	R Development Core Team	https://www.r-project.org/
cutadapt	Martin et al. ⁴⁵	https://cutadapt.readthedocs.io/en/stable/
STAR	Dobin et al. ⁴⁶	https://github.com/alexdobin/STAR
Htseq	Anders et al. ⁴⁷	https://htseq.readthedocs.io/en/latest/
DESeq2	Love et al. ⁴⁸	https://bioconductor.org/packages/devel/bioc/vignettes/DESeq2/inst/doc/DESeq2.html
DAVID	Huang et al. ⁴⁹	https://davidbioinformatics.nih.gov/
Cell Ranger	10X Genomics	N/A
Seurat	Butler et al. ⁵⁰	https://satijalab.org/seurat/
RECODE	Imoto et al. ⁵¹	https://github.com/yusuke-imoto-lab/RECODE
GSEA	Subramanian et al. ⁵²	https://www.gsea-msigdb.org/gsea/index.jsp
Other		
Mm-H2-Aa RNA probe	Advanced Cell Diagnostics	841761
Mm-Ceacam10 RNA probe	Advanced Cell Diagnostics	424581
Mm-Ly6e RNA probe	Advanced Cell Diagnostics	802921
Mm-Reg1 RNA probe	Advanced Cell Diagnostics	511571
Mm-Apoa1 RNA probe	Advanced Cell Diagnostics	807151
Mm-Chga RNA probe	Advanced Cell Diagnostics	447851

EXPERIMENTAL MODEL AND STUDY PARTICIPANT DETAILS

Mouse husbandry

Wild type mice and *Lgr5*-eGFP-IRES-CreERT2 mice¹ (Jackson Laboratories, JAX 008875) were maintained on the C57BL/6J background. Age was classified as follows: young (2-4 months of age), middle-aged (11-18 months of age), aged (22-27 months of age) and super-aged (28-30 months of age). The sex of the mice used in the experiments is described in the figure legends. Mice were housed in the conventional animal facility under a 12-h light/12-h dark cycle. All animal experiments were conducted in accordance with the Regulation on Animal Experimentation at Kyoto University and approved by the Animal Experimentation Committee of Kyoto University.

Small intestinal organoid culture

The proximal half of the small intestine was dissected, washed with cold PBS (Mg-/Ca-) and opened. Villi were removed by scraping with glass slides. The tissues were cut into 3-5 mm fragments and washed 5-6 times in cold PBS (Mg-/Ca-) with gentle shaking by hand. The pieces were then incubated for 30 min at 4°C in PBS (Mg-/Ca-) containing 5 mM EDTA. Crypts were then mechanically isolated by vigorous shaking and filtered through a 70- μ m mesh to remove remaining villus and tissue fragments. Isolated crypts were counted and embedded in Matrigel (Corning, 356231) at 10 crypts per μ L. Twenty-five microlitres drops of Matrigel with crypts were plated on a 48-well plate (Iwaki, 3830-048) and cultured in advanced DMEM/F12 (Thermo Fisher Scientific, 12634) medium containing 1X GlutaMax (Thermo Fisher Scientific, 35050), 10 mM HEPES (Thermo Fisher Scientific, 15630), 100 U/mL penicillin/streptomycin (Thermo Fisher Scientific, 15140122), 1X N2 supplement (Thermo Fisher Scientific, 17502), 1X B27 supplement (Thermo Fisher Scientific, 17504), 50 ng ml⁻¹ mouse recombinant EGF (R&D Systems, 2028), 100 ng ml⁻¹ mouse recombinant

Noggin (PeproTech, 250-38), 500 ng ml⁻¹ human recombinant R-spondin-1 (R&D Systems, 4645-RS), and 1 μ M *N*-acetyl-L-cysteine (Sigma–Aldrich, A9165). Then, 10 μ M Y27632 (WAKO, 257-00511) was added for the first two days. The medium was changed every other day. The intestinal organoids have not been authenticated, and they have not been tested for mycoplasma contamination.

METHOD DETAILS

5-FU injection to mice

5-FU (Sigma–Aldrich, F6627) was injected intraperitoneally at 200 mg/kg body weight, and the intestine was harvested 72 hours after 5-FU injection.

EdU injection to mice

EdU (Thermo Fisher Scientific, A10044) was injected intraperitoneally at 80 mg/kg body weight, and the intestine was harvested 48 hours after EdU injection.

Tissue sample preparation and phenotypic analysis

Small intestine specimens were washed with cold phosphate-buffered saline (PBS). For immunohistochemistry, immunofluorescence, EdU staining and alcian blue staining, proximal regions (6–9 cm from the start of the small intestine) were fixed overnight in 4% paraformaldehyde in PBS at 4°C or in 10% neutral buffered formalin (NBF) at room temperature. For Figure S4F, the proximal half of the small intestine was rolled up longitudinally and fixed overnight in 10% NBF at room temperature. The fixed tissues were dehydrated, embedded in paraffin and sectioned at 4–6 μ m thickness by the Center for Anatomical, Pathological and Forensic Medical Research, Kyoto University Graduate School of Medicine. The sections were deparaffinized and rehydrated. Antigen retrieval was performed by boiling samples for 20–40 min in 10 mM Tris-HCl buffer at pH 9.0 containing 1 mM EDTA (Agilent, S2367) or 10 mM citrate buffer at pH 6.0 (Agilent, S1699). The sections were incubated with the following primary antibodies at 4°C overnight: anti-Ki67 (Abcam, ab15580; dilution 1:1000), anti-Olfm4 (CST, 39141; dilution range 1:200–1:400), anti-CD4 (Abcam, ab108508; dilution 1:1000), anti-Lyz1 (Abcam, ab108508; dilution 1:400), anti-Chromogranin A (Chga) (Abcam, ab15160; dilution 1:400), anti-Dclk1 (Abcam, ab37994; dilution 1:50), anti-phospho-ERK1/2 (CST, 4376; dilution 1:400) and anti-E-cadherin (BD Biosciences, 610181; dilution range 1:200–400). For immunohistochemistry, the sections were incubated with peroxidase-conjugated secondary antibodies (Vector Labs, Vectastain Elite ABC or Nichirei Biosciences, Histofine) at room temperature for 30 min, and chromogen development was performed using DAB (Vector Labs or Nichirei Biosciences). The stained slides were counterstained with haematoxylin. For immunofluorescence, Alexa Fluor 488-, Alexa Fluor 594- and Alexa Fluor 633-conjugated anti-rabbit or anti-mouse secondary antibodies (Thermo Fisher Scientific, dilution range 1:200–1:500) were used. The stained slides were counterstained with Hoechst 33342 (Thermo Fisher Scientific H3570). EdU staining was performed by using the Click-iT EdU Alexa Fluor 488 Imaging Kit (Thermo Fisher Scientific, C10337) according to the manufacturer's instructions. For goblet cell analysis, sections were stained with Alcian blue solution (Nacalai, 37154) and counterstained with nuclear fast red (Scytek Laboratories, NFS125). Crypt height and villus length were measured using ImageJ software (NIH)⁴⁴ based on images of HE-stained sections. More than 30 crypts or 10 villi per mice were evaluated. For quantification of Ki67, Olfm4 and EdU (4 hours of incorporation) staining, we calculated the number of positive cells per crypt. More than 25 crypts per mouse were evaluated. To assess the migration rate of intestinal epithelial cells, the distance from the crypt/villus boundary to the tip of EdU-positive cells at 48 hours post-EdU treatment was measured using ImageJ. More than 24 crypt-villus axes per mouse were measured. For quantification of Chga, alcian blue and Dclk1 staining, the number of positive cells from 3–4 small intestine transverse sections per mouse was measured and divided by the total area of the tissue. For quantification of CD4 staining, the number of CD4-positive cells in the crypt surrounding area from 3–4 small intestine transverse sections per mouse was measured and divided by the crypt area. For assessment of phospho-ERK1/2 levels (Figure 4G), all crypts from 3–4 small intestine transverse sections per mouse were analysed based on the criteria shown in the figure legend.

Flow cytometry

The isolated crypts were dissociated into single cells by treating the cells with TrypLE Express (Thermo Fisher Scientific, 12604013) containing DNase I (10 U μ L⁻¹, Roche, 4716728001) for 30 min at 37°C and gentle pipetting. The dissociated cells were resuspended in cold MEM (Thermo Fisher Scientific, 11380037) and incubated with the following antibodies for 30 min at 4°C: EPCAM-APC (G8.8) (BioLegend, 118213) and CD24-Pacific Blue (M1/69) (BioLegend, 101819), both at 1:500. Finally, the cells were resuspended in MEM supplemented with 7-AAD (BD Biosciences, 559925, dilution 1:100), 100 U mL⁻¹ RNase inhibitor (Thermo Fisher Scientific, 10777019) and 10 μ M Y27632 (Tocris Bioscience, 1254). Cells were sorted using a FACS Aria II or FACS Aria IIu (BD Biosciences). ISCs were isolated as *Lgr5*GFP^{high}Epcam^{high}CD24^{low}7-AAD⁻, progenitors were isolated as *Lgr5*GFP^{medium/low}Epcam^{high}CD24^{low}7-AAD⁻, and Paneth cells were isolated as CD24^{high}Sidescatter^{high}*Lgr5*GFP⁻Epcam^{high}7-AAD⁻. The gating strategies are shown in Figure S1E. For cell preparation for single-cell RNA-seq analysis, the following antibodies were added to remove leukocytes, erythroid cells and endothelial cells, all at 1:500: CD45-PE/Cy7 (30-F11) (BioLegend, 103113), Ter119-PE/Cy7 (TER-119) (BioLegend, 116221) and CD31-PE/Cy7 (Mec13.3) (BioLegend, 102523). Intestinal epithelial cells were isolated as Epcam^{high} CD31⁻ Ter119⁻ CD45⁻ 7-AAD⁻ cells. Data were analysed using FACSDiva and FlowJo (BD Biosciences).

RNA *in situ* hybridization

RNA *in situ* hybridization was performed with RNAScope Multiplex Fluorescent v2 (Advanced Cell Diagnostics, 323100) according to the manufacturer's instructions. The following probes were used: *H2-Aa*, Mm-H2-Aa, #841761; *Ceacam10*, Mm-Ceacam10, *Ly6e*, Mm-Ly6e, #802921; *Reg1*, Mm-Reg1, #511571; *Apoa1*, Mm-Apoa1, #807151; *Chga*, Mm-Chga, #447851. For the quantification of RNA *in situ* hybridization in [Figure 2I](#), 3-4 small intestine transverse sections were imaged at 40X magnification with an Eclipse Ti2 microscope (Nikon). The mean signal intensity in each villus axis was measured by using ImageJ software. More than 50 villi axes per mouse were measured. For the quantification of RNA *in situ* hybridization in [Figure 7D](#), stained samples were randomly imaged at 400X magnification with an Eclipse Ti2 microscope (Nikon). The mean signal intensity in each crypt was measured by using ImageJ software. Crypt cells were identified by E-cadherin staining. More than 20 crypts per mouse were measured.

Intestinal organoid treatments

In [Figure 4D](#), on the fourth day after plating, the following cytokines or small molecule compounds were added to the intestinal organoid culture medium for 24 hours: mouse recombinant IFN- γ (PeproTech, 315-05), mouse recombinant IFN- α (BioLegend, 752802), mouse recombinant TNF- α (PeproTech, 315-01A), Pam3CSK4 (InvivoGen, tlr-pms), Poly (I:C) (Tocris Bioscience, 4287), LPS (Sigma-Aldrich, L4391), Retinoic Acid (Sigma-Aldrich, R2625), MHY1485 (Sigma-Aldrich, SML0810), EX527 (Santa Cruz, sc-203044), PD0325901 (Wako, 162-25291), and Etomoxir (Sigma-Aldrich, E1905). The final concentrations used in the experiments are as follows; IFN- γ , 0.05, 0.5 and 5 ng/mL; IFN- α , 0.1, 1 and 10 ng/mL; TNF- α , 1, 10 and 100 ng/mL; Pam3CSK4, 0.1, 1 and 10 μ g/mL; Poly (I:C), 1, 10 and 100 μ g/mL; LPS, 0.1, 1 and 10 μ g/mL; RA, 0.1, 1 and 10 μ M; MHY1485, 1, 3 and 10 μ M; EX527, 1, 10 and 100 μ M; PD0325901, 1, 3 and 10 μ M; Etomoxir, 100 and 200 μ M. All control organoids were treated with similar concentrations of the compound's dissolvent, dimethyl sulfoxide (Sigma-Aldrich, D2650), PBS and water. In [Figures S4C](#) and [S4E](#), 10 μ M JAK1/2 inhibitor, Ruxolitinib (Selleck, S1378) were added to the intestinal organoid culture medium for 1 hour followed by the addition of IFN- γ (0.5 ng/mL), IFN- α (1 ng/mL) or IFN- λ 3 (10 ng/mL, R&D Systems, 1789-ML). In [Figure S4G](#), 3 μ M PD0325901, 10 μ g/mL Pam3CSK4, 50 μ M p38/MAPK inhibitor SB203580 (Merck Millipore, 559389), 50 μ M JNK/MAPK inhibitor SP600125 (Merck Millipore, 420119) and 50 μ M NF- κ B inhibitor BAY 11-7082 (Selleck, S2913) were added to the organoid culture medium for 24 hours. Cell differentiation was induced by removing R-spondin1 and adding 2 μ M IWP2 (Selleck, S7085). In [Figure S5A](#), entire wells were imaged at 40X magnification with an Eclipse Ti2 microscope (Nikon) and stitched by NIS-Elements AR software (Nikon). For the quantification of organoid formation efficiency, the number of organoids per well was measured for 2-4 wells from each mouse and then divided by the initial crypt number. For the quantification of organoid size in [Figures 5A](#) and [S5B](#), live organoids embedded in Matrigel were randomly photographed at 100X magnification with an IX71 microscope (Olympus), and the area of the organoids was measured by using ImageJ software. In each independent biological experiment, more than 20 organoids per condition were evaluated. For EdU incorporation analysis in [Figures 5B](#) and [S5C](#), EdU (final 10 μ M) (Thermo Fisher Scientific, A10044) was added to the culture medium for 2 hours and fixed overnight with 4% paraformaldehyde in PBS at 4°C. EdU staining was performed by using the Click-iT EdU Alexa Fluor 488 Imaging Kit (Thermo Fisher Scientific, C10337) and imaged using an FV3000 confocal microscope (Olympus). The number of EdU-positive cells was counted and divided by the circumference of the organoids. In each independent biological experiment, 10-35 organoids per condition were evaluated. For Propidium Iodide (PI) staining, PI (final 10 μ g/mL) (Sigma-Aldrich, P-4170) were added to the culture medium for 30 minutes. For the quantification of organoid damage in [Figures 5C](#) and [S5D](#), both live and dead organoids were randomly photographed at 100X magnification with an IX71 microscope (Olympus), and the intact area (PI-negative area) of the organoids was measured by using ImageJ software and divided by the total area (PI-positive and -negative area). In each independent biological experiment, 10-35 organoids per condition were evaluated. For [Figure 6G](#), 50 μ M c-Myc inhibitor 10058-F4 (Selleck, S7153) were added to the PD0325901 and IFN- γ treated organoids for 24 hours. EdU staining was performed as mentioned above.

RT-qPCR

RNA from small intestine tissues (9-10 cm from the start of the small intestine) was isolated with a QIAshredder (Qiagen, 79656) and RNeasy mini kit (Qiagen, 74106) according to the manufacturer's instructions. Cultured intestinal organoids were harvested using Cell Recovery Solution (Corning, 354253), and RNA was isolated with an RNeasy micro kit (Qiagen, 74004) according to the manufacturer's instructions. Isolated RNA was transcribed with a QuantiTect reverse transcription kit (Qiagen, 205311). Quantitative PCR analyses were performed by using a StepOnePlus (Applied Biosystems) with SYBR Premix Ex TaqII (Takara, RR820). Each value obtained was normalized to *Actb* or *Hprt*. Primer sequences are listed in [Table S7](#).

Library preparation for bulk population RNA-seq in [Figure 1](#)

The cells were lysed, and the total RNA was purified using an RNeasy Micro Kit (Qiagen, 74004) according to the manufacturer's instructions. One nanogram of total RNA from each sample was used for the synthesis and amplification of cDNA according to the single-cell 3 prime RNA-seq (SC3-seq) method described previously^{53,54}. For RNA-seq libraries of Paneth cell samples, technical replicates were prepared. RNA-seq libraries were sequenced on a NextSeq 500 (Illumina) with a NextSeq 500 High Output v2 Kit (Illumina, FC-404-2005). The sequences of oligonucleotides used in the SC3-seq methods are listed in [Table S7](#).

Bulk population RNA-seq data analyses in Figure 1

The sequenced reads were trimmed to remove low-quality bases and adaptor sequences using cutadapt v3.0⁴⁵. The sequenced reads were mapped to the mm10 mouse reference genome using STAR v2.7.9a⁴⁶ with the GENCODE vM23 annotation gtf file. The reads mapped to multiple genomic loci and to the mitochondrial genome were excluded from further analyses. The read counts per gene were calculated using HTSeq-count v0.13.5⁴⁷. Each gene expression level was calculated as reads per million mapped reads (RPM) using DESeq2 v1.30.1⁴⁸. Principal component analysis (PCA) was performed using the R software package v4.0.3 using the genes with RPM > 1 in at least one sample. Differential expression analysis was performed by DESeq2 using the Wald test. The p values were corrected for multiple testing using the Benjamini and Hochberg method and represented as the false discovery rate (FDR). Genes upregulated with age were identified with FDR < 0.1, fold change (aged/young) > 1.5, and average RPM in aged samples > 10. Downregulated genes were identified with FDR < 0.1, fold change (young/aged) > 1.5, and average RPM in young samples > 10. Gene ontology analysis was performed using DAVID⁴⁹. Upstream regulator analysis was performed using IPA (QIAGEN) software.

Library preparation for single-cell RNA-seq

Intestinal epithelial cells were loaded into a 10X Genomics Chromium system. The cells of each group (young and aged mice) were obtained from three individual mice and analysed on different chips. scRNA-seq libraries were prepared using Single Cell 3' Reagent Kits v3.1 (10X Genomics, 1000128) according to the manufacturer's instructions. The libraries were then sequenced on a NextSeq 500 (Illumina).

Analysis of the scRNA-seq data

scRNA-seq data were mapped against the mm10 reference genome and quantified using the Cell Ranger pipeline (v.6.0.1). The Seurat package (version 4.0.2, and version 4.3.0)⁵⁰ and R (version 4.0.3 or 4.2.3) were used for quality control, filtering, noise reduction, normalization, clustering analyses, and visualization. A total of 10,844 cells (5,135 and 5,709 cells from young mice and aged mice, respectively) with 1,000 < nFeature < 6,000, nCount < 50,000, and low mitochondrial gene expression (< 25%) were further analysed. A noise reduction method, RECODE (RECODE v.0.1.1, <https://github.com/yusuke-imoto-lab/RECODE>)⁵¹, was applied to the quality-filtered UMI count matrices of young and aged samples separately. Batch effect correction was performed using the Seurat FindIntegrationAnchors functions (reduction method: cca). The expression levels were normalized using the log-normalization method in the Seurat package. The ScaleData function with the vars.to.regress option in the Seurat package was used to remove uninteresting sources of variation (total counts, percent of mitochondrial transcripts and cell cycle phases). UMAP analysis and clustering were performed using the Seurat RunUMAP function with default parameters (dims = 1:50) and the FindClusters function, with a resolution of 0.4. The cell type was annotated according to the expression of well-known markers. Differential expression analysis was performed by the Seurat FindMarkers function (default setting) using the Wilcoxon rank-sum test. The p values were corrected for multiple testing using the Bonferroni method and are represented as adjusted p values. Adjusted p values < 0.05 were considered significant. The detailed method used to identify cell type-specific genes is described in the Table S2, "Summary" sheet. Gene ontology analysis was performed using DAVID, and upstream regulator analysis was performed using IPA software. Cell cycle scores were calculated by the Seurat AddModuleScore functions (default setting) using the G1/S and G2/M gene sets⁵⁵. Cell-type scores were calculated by the Seurat AddModuleScore functions (default setting) using the cell type-specific expressed gene sets shown in Table S2. For calculation of the stem cell score, MHC class II genes (*H2-Aa*, *H2-Ab1*, *H2-Eb1* and *Cd74*) were excluded from the gene sets. Gene set enrichment analysis (GSEA) was performed using the GSEA v4.3.2 software package⁵². The log fold change values between young and aged cells in the mature enterocyte cluster were queried against previously published gene sets from different areas of the small intestinal crypt villus axis²⁵.

Integrative analysis of the three scRNA-seq datasets

scRNA-seq datasets from our study, Omrani et al. (GEO:GSE129710)¹⁸, and Funk et al. (GEO:GSE190848)²⁶, were mapped against the mm10 reference genome and quantified using the Cell Ranger pipeline (v.6.0.1). The Seurat package (version 4.4.0 and version 4.3.0)⁴⁹ and R (version 4.3.2 or 4.2.3) were used for quality control, filtering, noise reduction, normalization, clustering analyses, and visualization. Cells with 2,500 < nFeature < 8,000, 10,000 < nCount < 100,000, and low mitochondrial gene expression (< 25%) were further analysed. A noise reduction method, RECODE (RECODE v.1.0.0)⁵¹, was applied to the quality-filtered UMI count matrices of young and aged samples from each study separately. Batch effect correction was performed using the Seurat FindIntegrationAnchors functions (reduction method: cca). The expression levels were normalized using the log-normalization method in the Seurat package. The ScaleData function with the vars.to.regress option in the Seurat package was used to remove uninteresting sources of variation (total counts, percent of mitochondrial transcripts and cell cycle phases). UMAP analysis and clustering were performed using the Seurat RunUMAP function with default parameters (dims = 1:50) and the FindClusters function, with a resolution of 0.2. The cell type was annotated according to the expression of well-known markers. Differential expression analysis was performed by the Seurat FindMarkers function (default setting) using the Wilcoxon rank-sum test.

Library preparation for bulk population RNA-seq in Figure 6

Cultured intestinal organoids were harvested using Cell Recovery Solution (Corning, 354253), and RNA was isolated with an RNeasy micro kit (Qiagen, 74004). Total 100 ng RNA per sample were used for library construction. The RNAseq libraries were generated using the Illumina Stranded mRNA Prep, Ligation Kit (Illumina), according to the manufacturer's instructions. Sequencing was performed on an Illumina NextSeq 2000 platform with the paired-end mode.

Bulk population RNA-seq data analyses in Figure 6

The sequenced reads were mapped to the mm10 mouse reference genome using STAR (version 2.7.11a)⁴⁶, with the GENCODE M23 annotation gtf file after trimming adaptor sequences and low-quality bases by cutadapt-4.6⁴⁵. The uniquely and properly mapped reads were used for further analysis. The raw count matrix was created using htseq-count (version 2.0.5)⁴⁷ with GENCODE M23 annotation gtf file. Gene expression levels were determined as transcripts per million (TPM). Hierarchical clustering analysis was performed using the genes with TPM > 10 in at least one sample. Differential expression analysis was performed by DESeq2⁴⁸ using the Wald test. The p values were corrected for multiple testing using the Benjamini and Hochberg method and represented as the false discovery rate (FDR = q value). The genes whose expression values were upregulated by iMEK treatment (Log2FC (iMEK/Control) ≥ 1 , $q < 0.05$, average TPM in iMEK samples > 10), and its increases were enhanced or inhibited ($\geq 50\%$, $q < 0.05$) by the additional IFN- γ treatment, were defined as Group 1 or Group 2 genes, respectively. The genes whose expression values were downregulated by iMEK treatment (Log2FC (Control/iMEK) ≥ 1 , $q < 0.05$, average TPM in Control samples > 10), and its decreases were inhibited or enhanced ($\geq 50\%$, $q < 0.05$) by the additional IFN- γ treatment, were defined as Group 3 or Group 4 genes, respectively. The genes whose expression values were upregulated by IFN- γ treatment (Log2FC (IFN- γ /Control) ≥ 1 , $q < 0.05$, average TPM in IFN- γ samples > 10), and its increases were enhanced or inhibited ($\geq 50\%$, $q < 0.05$) by the additional iMEK treatment, were defined as Group 5 or Group 6 genes, respectively. The genes whose expression values were downregulated by IFN- γ treatment (Log2FC (Control/IFN- γ) ≥ 1 , $q < 0.05$, average TPM in Control samples > 10), and its decreases were inhibited or enhanced ($\geq 50\%$, $q < 0.05$) by the additional iMEK treatment, were defined as Group 7 or Group 8 genes, respectively. Gene ontology analysis was performed using DAVID⁴⁹. Upstream regulator analysis was performed using IPA (QIAGEN) software.

Data availability

RNA-seq and scRNA-seq data were deposited in the Gene Expression Omnibus under accession number GSE210242. The data will become public after the publication of our paper.

QUANTIFICATION AND STATISTICAL ANALYSIS

For all animal experiments, at least three different mice per condition were used. For analysis of *in vitro* organoid cultures, at least three independent biological experiments were performed with the exception of the screening assay (Figure 4D). The sample size and statistical test used for each quantification are indicated in the figure legends. No statistical method was used to predetermine sample sizes, but our sample sizes are similar to those reported in previous publications^{11–18,26}. Mice were randomly assigned to experimental groups. The investigators were not blinded to the allocation of samples during the experiments or outcome assessment. Statistical significance was analysed by two-tailed Welch's *t* test unless otherwise described. GraphPad Prism 8 or Microsoft Excel was used for statistical analysis. For Figures 2D, 2H, 3A, 4A, 4B, 5E–5K, 6B, 6D, 6H, S2E, S2F, S4A, S4B, S5E–S5K, S6A, and S6E, R (version 3.6.3 or 4.2.3) was used for visualization.